Synergy of active and passive airborne observations for heating rates calculation during the AEROCLO-SA field campaign in Namibia

Mégane Ventura[1], Fabien Waquet[1], Isabelle Chiapello[1], Gérard Brogniez[1], Frédéric Parol[1], Frédérique Auriol[1], Rodrigue Loisil[1], Cyril Delegove[1], Luc Blarel[1], Oleg Dubovik[1], Marc Mallet[2], Cyrille Flamant[3] and Paola Formenti[4].

[1]Laboratoire d'Optique Atmosphérique (LOA), Université Lille, CNRS, UMR 8518, 59000 Lille, France.

[2]Centre National de Recherches Météorologiques, UMR3589, Météo-France-CNRS, Toulouse, France.

[3]Laboratoire Atmosphères, Observations Spatiales (LATMOS), CNRS, Sorbonne Université, UVSQ, 75252 Paris, France.

[4]Université Paris Cité and Univ Paris Est Creteil, CNRS, LISA, F−75013 Paris, France

Correspondence to: Fabien Waquet (fabien.waquet@univ-lille.fr)

Abstract. Aerosols have important effects on both local and global climate, as well as on clouds and precipitations. We present original results derived from the airborne observations acquired from the AErosol RadiatiOn and CLOud in Southern Africa (AEROCLO-sA) field campaign led in Namibia in August and September 2017. In order to quantify the aerosols radiative impact on the Namibian regional radiative budget, we use an innovative approach that combines the OSIRIS polarimeter, airborne prototype of the future 3MI polarimeter of ESA and lidar data to derive heating rate of the aerosols. To calculate this parameter, we use a radiative transfer code, meteorological parameters provided by dropsondes and OSIRIS-retrieved aerosol optical thickness, size, and absorption above clouds. This approach is evaluated during massive transports of biomass burning particles above clouds. We present vertical profiles of heating rates computed in the solar and thermal parts of the spectrum. Our results indicated strong positive heating rate values retrieved above clouds due to aerosols, between +2 and +5 Kelvin per day (vertically averaged). Within the smoke layer, water vapor's cooling effect through infrared radiation generally balances its warming effect from solar radiation. At the top of the layer, a stronger cooling effect of -1.5 K/day often dominates due to water vapor. In order to validate this methodology, we use irradiance measurements acquired during spiral descent performed with the aircraft during dedicated parts of the flights, which provides direct measurements of irradiances distribution and heating rates in function of the altitude. Despite the challenges posed by cloud horizontal variability observed during the spiral descent, simulated and measured results generally agree in most cases. Finally, we discuss the possibility to apply this method to available and future spaceborne passive and active sensors.

1 Introduction

Aerosols particles, from both natural or anthropogenic sources, are complex components of the atmosphere with highly variable chemical, optical and microphysical properties. Aerosols directly impact the climate by interacting with the solar and terrestrial radiations. Depending on their properties and spatial distribution (e.g., above clouds or a dark surface), they can contribute to warming or cooling the planet by directly modifying its radiative balance (Solomon et al., 2007; Trenberth et al., 2009; Peers et al., 2016). These particles may also act as cloud condensation nuclei (or ice nuclei) and modify the cloud properties and lifetime and thereby indirectly influencing the radiative balance. Their effects on clouds and climate are still associated with large uncertainties, especially in case of aerosols situated within or above the clouds (Bellouin et al., 2020, IPCC, 2022).

The aerosol radiative forcing estimates provided by climate model over the Southeast Atlantic Ocean show large discrepancies (Zuidema et al., 2016a). This area is characterized by a persistent marine stratocumulus deck extending along the African coasts from Namibia to Gabon. During the fire season (from June to October), fires related to agricultural practices in Central Africa generate massive smoke plumes over the Tropical Africa (Redemann et al., 2021). These smoke plumes, carried across the Atlantic Ocean, travel above the stratocumulus clouds and may interact with them either at the cloud top (Bréon and Costantino, 2013) or below entering the marine boundary layer. These situations, as they represent a unique opportunity to study the complex interactions between biomass burning aerosols, clouds and radiation, have been the topic of a number of studies (Pilewskie et al., 2003; Keil and Haywood, 2003; Magi et al., 2008; Stier et al., 2013; Peers et al., 2016; Zuidema et al., 2016a; Zuidema et al., 2016b; Haywood et al., 2021). Biomass burning aerosols include black carbon, a compound that strongly absorbs radiation across a wide spectral range. Biomass burning particles also contain organic carbon, which may include brown carbon, a substance that makes organic carbon absorbing to radiation, particularly in the ultraviolet (Lack et al., 2012; Siméon et al., 2021). Biomass burning aerosols plumes transported above clouds are linked to a pronounced positive direct radiative forcing (warming), that is still underestimated in climate models (De Graaf et al., 2020). Recently, the latest generation of global climate models used in the CMIP6 modelling exercise have been shown to suffer in the representation of solar heating due to absorbing biomass burning aerosols (BBA) over the Southeast Atlantic (SEA) Ocean, due to underestimated aerosols absorption (Mallet et al., 2021). The absorption of solar energy by these aerosols alters the thermodynamic properties of the atmosphere, impacting the vertical development of low-level clouds, the subsidence of dry air from the free troposphere within the marine boundary layer (Johnson et al., 2004) and influencing cloud top height, water content and brightness (Lu et al., 2018). This aerosol semi-direct effect has been previously observed off the coasts of Angola (Wilcox, 2012; Deaconu et al., 2019). In addition, the semi-direct effect of BBA on the low-level clouds has been also reproduced with global or regional climate models, showing a general increase of low-level cloud fraction due to BBA (Sakaeda et al., 2011; Mallet et al., 2020).

This study focuses on quantifying the radiative impact of biomass burning aerosols and aims to estimate the profiles of atmospheric heating (or cooling) rates attributable to these particles. We use airborne measurements acquired during the

AErosols Radiation and CLOuds in southern Africa (AEROCLO-sA) campaign (Formenti et al., 2019) conducted over Namibia between 5 and 12th September 2017 with the French Falcon 20 environmental research aircraft of Safire. During AEROCLO-sA, massive plumes of BBAs were observed traveling over the Namibian deserts and above the coastal stratocumulus clouds (Chauvigné et al., 2021). In parallel, other international campaigns have been also conducted in this Southeast Atlantic area, such as ORACLES (ObseRvations of Clouds above Aerosols and their inteEractionS) by NASA (Redemann et al., 2021) and the CLARIFY (Cloud-Aerosol-Radiation Interactions and Forcing: Year 2016) project (Haywood et al., 2021). The aerosol heating rate is a radiative quantity (measured in Kelvin per unit time) that represents the ability of aerosol particles to heat or cool the atmospheric layer in which the aerosols are located. Quantifying these heating rates is crucial to understand the impact of smoke aerosols on the of low-level cloud properties and on the atmospheric dynamic over the tropical African region. Recent studies have emphasized the importance of accurate heating rate knowledge for proper modeling of the transport and dynamics of biomass burning aerosol layers (Chaboureau et al., 2022). These biomass burning aerosols may also warm the lower troposphere sufficiently over the SEA to potentially impact West African monsoon dynamic and precipitation (Solmon et al., 2021).

However, accurately estimating aerosol heating rates remains a challenge due to their dependence on the aerosol concentration, but also their vertical and spatial distribution as well as their composition and size. In terms of optical parameters, the aerosol optical thickness (AOT) and the aerosol single scattering albedo (SSA) as well as their spectral dependence must be ideally known. The aerosol optical thickness depends on the particle's concentration whereas the SSA quantitatively describes the ability of aerosols to absorb or scatter the solar radiation. Given the same properties of aerosols (AOT, SSA and particles size), the extent of the heating rates is primarily determined by the brightness of the underlying clouds, which is a function of cloud optical depth. For accurate heating rate estimates, the vertical profiles of the thermodynamical quantities (humidity and temperature) also need to be known.

Among the different results obtained under the recent international projects, one important common finding is that the absorption by BBA appears to be very high over SEA with maximum absorption in August and minimum absorption in October (Wu et al., 2020; Pistone et al., 2019; Chauvigné et al., 2021; Jethva et al., 2024) with a column integrated SSA as low as ~0.85 (at 550 nm) or ~0.80 (at 865 nm) in August. Even lower SSAs were measured (in situ) within aged smoke layers (Zuidema et al., 2018; Denjean et al., 2020). These are clear indications that these smoke plumes have the ability to strongly absorb solar radiation and consequently heat the lower troposphere in this region.

Current innovative aerosol satellite observations are able to provide estimates of aerosol direct radiative forcing at the top of the atmosphere, even for aerosols layers located above clouds (Meyer et al., 2013; Peers et al., 2015; Zhang et al., 2016). However, such estimates do not capture the full impact of aerosols within the atmosphere or at the surface. Currently, the heating/cooling rate is not provided globally and operationally by satellites, although it is essential for understanding aerosols influences on atmospheric thermodynamic profiles and their semi-direct effects on clouds. Ongoing satellite products for above-cloud aerosols detection, like those from The Moderate Resolution Imaging Spectroradiometer (MODIS), and the Ozone Monitoring Instrument (OMI) on the A-Train constellation (Jethva et al., 2018) or the Spinning Enhanced Visible and Infrared

Imager (SEVIRI) on board the Meteosat Second Generation (MSG) satellites, (Peers et al., 2019), primarily focus on aerosol optical thickness (AOT) retrieved in the ultraviolet-visible-near-infrared (UV-VIS-NIR) range. Flying aboard PARASOL within the A-Train constellation (2005-2013), the *Polarization and Directionality of the Earth's Reflectances* (POLDER) instrument made multi-angular, multi-polarization, and spectral measurements, enabling the retrieval of more detailed information about the properties of aerosols above clouds including aerosol absorption (Waquet et al., 2009, 2013a; Peers et al., 2015, Waquet et al., 2020). Spaceborne lidars, like the Cloud-*Aerosol* Lidar with Orthogonal Polarization (CALIOP) on the A-Train, provides vertical profiles of aerosols. These instruments are particularly valuable for detecting aerosols above clouds, even though they offer limited information on the aerosols' detailed properties (Deaconu et al., 2017). If properly constrained, CALIOP vertical extinction profiles can provide altitude-dependent heating rates (Deaconu et al., 2019). Further work is therefore needed to document the semi-direct aerosol effect from satellite observations and this will necessarily include instrument synergy.

Airborne measurements are particularly useful for accessing the atmospheric heating/cooling rates. As they can be made at different levels in the atmosphere, they make it possible to obtain vertical profiles of atmospheric and aerosol properties. In the context of the ORACLES project (Redemann et al., 2021), aerosol heating rates above clouds were calculated from airborne measurements (Cochrane et al., 2022). In Cochrane et al. (2022), the authors rely on in-situ irradiance measurements made in smoke plumes at different altitudes to accurately characterize the extinction and absorption properties of aerosols, as well as thermodynamic profiles. These data, coupled with a radiative transfer code, allowed the calculation of heating rates in the shortwave visible. This latter study notably employs a synergistic approach, combining irradiance data from the Solar Spectral Flux Radiometer (SSFR), with airborne sun-photometer measurements of AOT from the Spectrometers for Sky-Scanning Sun-Tracking Atmospheric Research (4STAR) instrument and HSRL-2 lidar extinction profiles. The irradiances of SSFR were used to measure the below aerosol layer scene albedo. Measurements were performed over the South East Atlantic Ocean along the Namibia coast in September 2016 and further north in August 2017, since ORACLES was based in the Sao Tome Island in 2017. Cochrane et al. (2022) found strong heating rates values in the shortwave spectrum varying between 2 and 8 K per day depending on location and period.

Heating rates can be also estimated from the calculation of the divergence of the measured irradiances, as it has been done in the Mediterranean Sea (Mallet et al., 2016). However, the use of airborne irradiance measurements for the calculation of heating rates poses significant difficulties. These are related to different factors, as for instance accounting for the aircraft's attitude variations (pitch, roll, heading) and their effects in the analysis of the measured fluxes (Brogniez et al., 2025).

During AEROCLO-sA, several instruments were employed onboard the aircraft, especially the Observing System Including PolaRization in the Solar Infrared Spectrum (OSIRIS) polarimeter (Chauvigné et al., 2021), a prototype of the upcoming European Space Agency's 3MI spaceborne instrument (Fougnie et al., 2018), and the LNG lidar. In the present study, the evaluation of the profiles of aerosol heating rates is achieved by assimilating airborne polarimeter OSIRIS and lidar LNG data into a radiative transfer code. This synergy of active and passive measurements is used to provide profiles of aerosol heating rates computed above low-level clouds in the solar and thermal infrared spectral domain. The calculation of

atmospheric heating rates (including aerosol, water vapor and other gas) is also discussed. An innovative aspect of our approach lies in utilizing the measurements obtained during spiral descents performed with the F-20 aircraft, particularly irradiance measurements acquired from pyranometer and pyrgeometer, in order to validate the calculated heating/cooling atmospheric rates and the overall methodology.

135   The paper is organized as follows. Section 2 describes the main flight's patterns and the instruments used in our study. Section 3 explains the method and how irradiance measurements are used to calculate atmospheric heating rates and details the validation processes of our methodology. Section 4 presents the findings from using both active and passive data to quantify aerosol heating rates above clouds throughout the campaign. Section 5 summarizes the key results and main perspectives.

2 Field campaign

140   ### 2.1 Flight patterns and general campaign description.

The AEROCLO-sA airborne campaign consisted of ten flights departing from Walvis Bay Airport in Namibia between 5 and 12th September 2017. During the campaign, the air mass intercepted (or measured) by the on-board instruments were mainly transported from the in-land biomass burning source areas, emitting substantial amounts of carbonaceous aerosols transported over the southeastern Atlantic Ocean, as far as the Ascension Island. The airmass was then drifted to the southeast towards the

145   Namibian coast due to the anticyclonic circulation located over South Africa (Chauvigné et al., 2021). These meteorological conditions were those encountered throughout the campaign except for 5th September (see Figure 2 in Chauvigné et al., 2021); the anticyclone was then positioned further east, between the coasts of South Africa and Madagascar, which led to a greater transport of biomass burning aerosols over the continent (i.e. transport over land from the source areas).

150
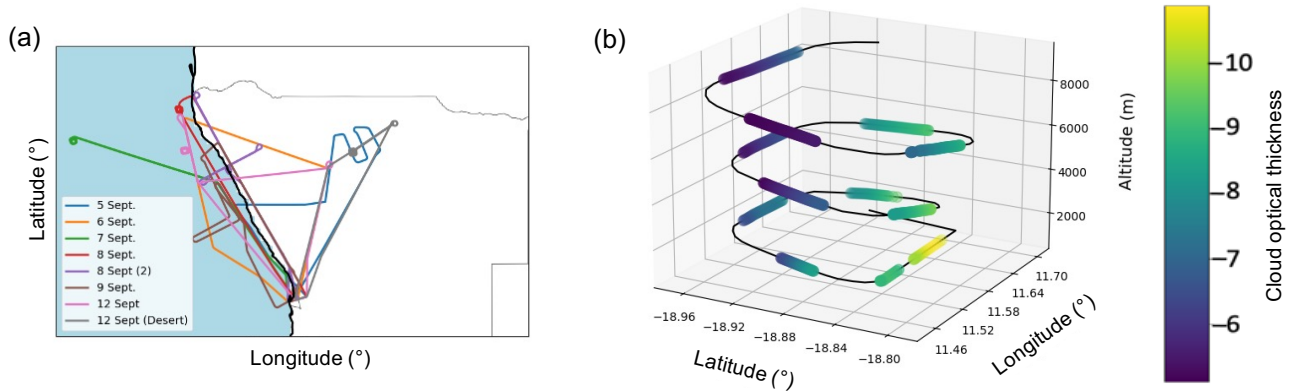
Figure 1: (a) Map of flight plans during the AEROCLO-sA campaign in Namibia between 5th and 12th September, 2017. (b) Example of an aircraft trajectory for a profile. This profile was performed on 12th September. The cloud optical thickness retrieved at 550 nm is also reported (color scale). The method used to retrieve the COD is described in section 3.3.2.

Figure 1 shows the trajectories of the flights, which were mainly carried out along the Namibian coast and over the Namibian deserts. The flight segments used in this study were solely performed over the ocean under cloudy conditions. The circles represent spiral descents performed with the aircraft during some of the flights. These descents make possible to obtain vertical profiles of the properties of the atmosphere over a restricted geographical area. The radius of these spirals is of the order of ten kilometers (see Figure 1b). They were carried out between 1 and 8 km altitude and lasted an average of 20 to 30 minutes. To minimize the influence of aircraft attitude on the data, pilots actively controlled pitch and roll during specific descent segments. This reduces aircraft tilt, transforming the originally spiral trajectory into a more controlled, hippodrome-like path (Figure 1b). In addition, round-trip flight segments were also performed during one specific flight in the solar plane and perpendicular to the solar plane in order to accurately determine the instrument's position within the aircraft for further data correction (Brogniez et al., 2025).

Date	Comments	Time (UTC)	Aerosol and cloud mean properties			
			COT (at 550 nm)	ImRI (at 865 nm)	AOT (at 865 nm)	MODE (in microns)
5/09		9h31-9h54	3-11	0.018	0.40	0.10-0.12
6/09	Thin clouds	8h44-8h48	1,5-3	0.026	0.57	0.10
7/09		9h32-10h36	8-18	0.035	0.18-0.30	0.12
7/09	Spiral descent	10h36-10h57	9-23	0.024	0.22	0.12
8/09		7h45-8h13	5-25	0.027	0.40-0.50	0.10-0.12
8/09	Spiral descent	8h13-8h33	7-16	0.022	0.45	0.12
9/09		7h57-9h15	4-10	0.030	0.25-0.35	0.12
12/09		7h23-8h24	2-20	0.028	0.11-0.20	0.10-0.12
12/09	Spiral descent	8h24-8h42	7-16	0.024	0.22	0.12

Table 1: Summary of the main characteristics of the flight segments with aerosol above clouds scenes, as observed during the AEROCLO-sA campaign, focusing on average properties (or min and max values) of aerosols and clouds retrieved by the OSIRIS instrument (Chauvigné et al., 2021). "Spiral descent" indicates that an aircraft sounding (i.e., rapid descent of the aircraft) was performed during the flight. COT refers to Cloud Optical Thickness at 550 nm, ImRI stands for the imaginary part of the complex refractive index at 865 nm, AOT refers to Aerosol Optical Thickness at 865 nm (AOT values of > 0.4 at

865 nm translate to AOT of > 1 at 500 nm) and MODE indicates the mean radius of the particles size distribution assuming a lognormal particle size distribution (by number) as retrieved from the polarimetric measurements provided by OSIRIS (Chauvigné et al., 2021).

175

Table 1 presents the characteristics of the flight segments used in our study. The aerosol and cloud parameters in table 1 were obtained from the OSIRIS data (Chauvigné et al., 2021). Some information on the flights are also reported. Aerosol optical thickness exhibits significant variability, with the most aerosol-laden events occurring primarily during the first phase of the campaign. Flights conducted on 5, 6 and 8th September show particularly remarkable atmospheric optical thickness (AOT) values at 865 nm, with values above 0.4. Associated aerosol properties retrieved by OSIRIS show minimal variation in size and imaginary refractive index (ImRI) of aerosol (ImRI $\approx 0.025 \pm 0.005$ and granulometric radius around 0.10 ± 0.02 microns).

2.2 Instrumentation onboard the Falcon 20.

During AEROCLO-sA, the Falcon 20 aircraft carried a suite of instruments, including a lidar, a polarimeter, a sun-photometer, particle probes, cloud microphysics probes, and sensors for irradiance measurements. OSIRIS, an acronym for Observing System Including PolaRisation in the Solar Infrared Spectrum, is an airborne imaging polarimeter designed to measure the spectral, directional, and polarized radiances (Chauvigné et al., 2021) serving as the airborne prototype for the future European Space Agency (ESA) spaceborne *Multi-viewing Multi-channel Multi-polarisation Imager* (3MI) instrument. The Stokes parameters are measured in 13 spectral channels (0.44 – 2.2 microns) and are used here to retrieve aerosol parameters (integrated over the column) above clouds. This instrument provides 20-meter resolution images for visible and near-infrared light (440-940 nm) and 60-meter resolution images for shortwave infrared light (940-2200 nm) at a 10-kilometer altitude.

The Leandre Nouvelle Génération (LNG) lidar provides the aerosol backscatter coefficient at different wavelengths in the ultraviolet (355 nm), visible (532 nm), and near infrared (1064 nm) that is used to depict the aerosol vertical distribution (Flamant et al., 2022). In our study, we use lidar LNG to depict the vertical profiles of aerosol extinction below the aircraft. A method of the type described in Klett et al., (1981) was used to solve the lidar equation. Biomass burning aerosols over the South East Atlantic Ocean often show particularly strong extinction at ultraviolet and shortest visible wavelengths. This leads to high optical thicknesses in these plumes, significantly weakening the lidar signal measured at 532 nm (or 355 nm). Consequently, lidar data acquired for optically thick plumes at these wavelengths become less reliable in accurately determining the base altitude of the aerosol layer (Jethva et al., 2014; Deaconu et al., 2019). On the other hand, the 1064-nm signal penetrates deeper into the aerosol layer due to significantly reduced attenuation, providing a better view of the depth of the aerosol layer. For this reason, we used LNG lidar data acquired at 1064 nm to accurately depict the aerosol extinction profile.

The PLASMA (Photomètre Léger Aéroporté pour la Surveillance des Masses d'Air) is an instrument designed to measure the aerosol optical thickness of extinction for the atmospheric column above the aircraft (Karol et al., 2013). It operates in ten spectral bands (340-1640 nm). One extra channel centered on 910 nm is also used to measure the water vapor amount.

Two CGR-4 pyrgometers and two CMP-22 pyranometers manufactured by Kipp and Zonen (K&Z) were installed on the top and bottom of the Falcon F20 fuselage during the AEROCLO-sA campaign (Brogniez et al., 2025). The CMP-22 pyranometer integrates irradiance over a wide spectral band covering the 297-3100 nm region. The CGR4 pyrgometer measurement is also integrated over a wide spectral band covering the 4.5-40 µm region. These data are used to directly measure the heating/cooling rates profiles within the biomass burning aerosol layers.

In addition to these remote sensing instruments, the aircraft was equipped with probes to measure thermodynamic quantities (temperature, pressure, wind and humidity). Dropsondes were also released. The particle size distribution of aerosols was also measured in situ during the flight with an Ultra High Sensitivity Aerosol Spectrometer (UHSAS) instrument (Formenti et al., 2019).

2.3 Case studies

Two flights were chosen (on 8th and 12th September, respectively) to assess our methodology. These flights exhibited large and moderate aerosol loading, respectively (see table 1 for AOT), with both flights incorporating a high-altitude transect and a spiral descent over a low-level cloud. Figure 7-a and 7-b show the attenuated backscattered coefficient retrieved by lidar LNG at 1064 nm for the selected flights.. During the flight on 8th September, a thick layer of biomass burning plume was observed above the stratocumulus clouds. The stratocumulus cloud top altitude was detected at approximately 600 m above the sea level, whereas white areas in Figure 7-a at 6 km altitude indicate high level-clouds. High relative humidity values were frequently measured near the smoke plume's uppermost layer, causing the hygroscopic growth of aerosols and sometimes cloud formation. Note that OSIRIS retrievals were screened for high-level clouds and that this instrument allowed aerosol characterization beyond the lidar's limited field of view (Chauvigné et al., 2021). In Figure 7-a and 7-b, note that the attenuated backscattering coefficient is shown only when lidar-derived aerosol extinction profile is also available. Compared to the flight on 12th September, the increased number of missing lidar retrievals (in white in Figure 7-a) observed on the 8th September flight is attributed to clouds forming at the top of the biomass burning layer. On the 12th September flight, the aerosol layers were less distinct, with particles distributed between the cloud top, which reached around 1,000 meters, and an altitude of 6 kilometers (Figure 7-b). In both cases, the sounding associated with the aircraft's spiral descent was made just after the measurements portions of flight presented in Figures 7a and 7b.

3 Method

3.1 Synergy of active, passive and thermodynamical measurements

235   The core of the method lies in leveraging the capabilities of both OSIRIS (passive) and the LNG lidar (active) instruments. This approach additionally incorporates other relevant measurements and retrieved quantities, acquired during the airborne campaign, as inputs for a radiative transfer code. The calculations of heating/cooling rates are performed in real time for each extinction profile provided by the lidar and when OSIRIS data are available.

      Our approach assumes that the inherent aerosol properties (imaginary refractive index and size retrieved by OSIRIS)

240   exhibit minimal variation with altitude above the cloud layer. Consequently, only the above clouds aerosol concentration is expected to vary with altitude, as reflected by the variation in the aerosol extinction profile. In our method, the lidar extinction profile is adjusted based on OSIRIS retrievals as follows:

$$ext_{1064nm}(z) = ext_{1064nm,lidar}(z) * \frac{\tau_{1064nm,OSIRIS}}{\tau_{1064nm,LNG\ lidar}} \qquad \text{(Eq. 1)}$$

245

With τ representing the aerosol optical thickness of the aerosol layer above clouds.

This correction (Eq. 1) is primarily used to ensure consistency between the optical properties retrieved by the lidar and those provided by OSIRIS. We also assume that the lidar accurately measures the base and top altitudes of the smoke layer, and that smoke aerosols are primarily confined within this range, typically between the cloud top and 6 km (see Figures 7a and 7b). To

250   determine the specific humidity profile for water vapor, combined data from onboard probes and dropsondes are used. Dropsonde measurements are used to set the qualitative shape of the specific humidity profile in the low cloud and a simple assumption is considered to obtain profile continuity with the onboard probes' measurements (see Figure 4d). The nearest available dropsonde is typically used. PLASMA measurements complement these by providing additional data for the region above the aircraft. PLASMA measurements confirmed that the integrated water vapor content above the aircraft at high altitude

255   was very low for all flights and we therefore considered it to be zero above the aircraft.

Table 2 summarizes the various instruments, along with the corresponding input parameters used in our methodology.

Instruments	Parameters
OSIRIS polarimeter	-Aerosol optical thickness at 865 nm -Imaginary part of the complex refractive index of aerosols (i.e. aerosol absorption) -Aerosol size

LNG lidar	-Extinction coefficient profile at 1064 nm -Cloud top altitude
PLASMA sun-photometer	-Integrated amount of water vapor above the aircraft
Dropsondes and aircraft sondes	-Temperature and pressure -Relative humidity
Pyranometer	-Cloud optical thickness at 550 nm

Table 2: Instruments and associated parameters used as input for the GAME code to compute irradiances and heating rates.

3.2 Radiative transfer code

260   The Global Atmospheric Model (GAME) allows calculating irradiance profiles with high spectral resolution (Dubuisson et al., 2006). The code considers 208 spectral intervals distributed between 0.2 and 3 µm for the solar spectrum. For thermal infrared, 115 intervals are used to cover the wavelength range from 4 microns to 47 microns. The model accounts for the most important absorbing gases, including water vapor. The model uses around 100 vertical layers. Vertical resolution was enhanced between 0 and 8 km, with a spacing of 100 meters. GAME utilizes various atmospheric models (temperature, pressure, etc.).

265   In our study, a tropical model is employed for the calculations. The water vapor profile is determined from probes' measurements. The total ozone content was adjusted using OMI space-based observations obtained for the campaign period. GAME integrates the obtained upward and downward irradiances (in W.m^{-2}) to compute the net irradiances (calculated between downward and upward irradiances) and heating/cooling rates over the solar or the thermal infrared spectrum.

The spectrally integrated heating/cooling rate (in Kelvin per day, K.day^{-1}) for an infinitesimal atmospheric layer dz at altitude

270   z is given by the general formula:

$$\frac{dT}{dt} = -\frac{1}{\rho C_p}\frac{dF_{net}(z)}{dz} \qquad \text{(Eq. 2)}$$

where C$_P$ stands for the specific heat capacity of air (J.kg^{-1}.K^{-1}) and ρ is the air density (Kg. m^{-3}). These quantities vary with

275   altitude and can be estimated from either atmospheric models or aircraft probes' measurements.

3.3 Aerosol and clouds properties

3.3.1 OSIRIS polarimeter retrieval

The retrieval algorithm for OSIRIS builds upon the same principle used by the POLDER spaceborne polarimeter to detect aerosol properties above clouds (Waquet et al., 2009, 2013a, Peers et al., 2015). The aerosol retrieval is based on solar plane

280   measurements and assumes spatial homogeneity over the entire OSIRIS visible image (an area of 20x10 km²). This procedure

increases the sensitivity to aerosol properties, which are retrieved at this spatial resolution using an optimal estimation method (Chauvigné et al., 2021). The method retrieves the column-integrated AOT, SSA, and imaginary part of the complex refractive index (i.e. representing aerosol absorption) in the visible spectral range. The optimal estimation method also provides uncertainties on these parameters (see Appendix A). The aerosol optical properties (integrated over the column), retrieved by

285   OSIRIS, are used as input for the radiative transfer code GAME. The OSIRIS algorithm and GAME calculations assume both a simplified aerosol representation: the real part of the complex refractive index is constant (1.47) across the spectrum and the imaginary part is independent of wavelength. This assumption implies that our simulation neglects the contribution of brown carbon. Consequently, we assume here that soot exclusively governs the absorption properties of aerosols generated from biomass burning. A single lognormal particle size distribution is used for which the mean radius is retrieved whereas the

290   variance is fixed (Chauvigné et al., 2021). The method directly retrieves the AOT, the mean radius and the imaginary part of the refractive index. The SSA is computed from the retrieved particles size distribution and the complex refractive index of the particles. The spectral range of the aerosol optical properties is broadened using Mie calculations to encompass both the thermal infrared and shortwave domains utilized by the GAME code.

3.3.2 Retrieval of cloud optical thickness from pyranometer measurements

295   Despite OSIRIS measurements allows for clouds properties retrievals, the use of cloud optical thicknesses retrieved from the pyranometer was favored in the rest of this study. Irradiance measurements integrate contributions from a spatially extended scene, making them more suitable for defining the average cloud albedo of the overlying cloud scene. The analysis employs a Look Up Table (LUT) method where the LUT was calculated with the GAME code. The retrieval takes into account the presence of the aerosol layer in the simulations in order to accurately retrieve the cloud properties. The simulation table

300   contains the following variables: zenith angle, COT, AOT, imaginary refractive index of the particles and altitude. The aerosol size distribution is fixed from the OSIRIS retrievals performed for each considered flight (Chauvigné et al., 2021). The vertical distribution of aerosol extinction follows that given by the lidar. A two-parameter gamma distribution was employed to describe the particles size distribution of cloud water droplets in the cloud layer situated below the aerosol layer. The effective radius and variance of the droplets were fixed at 10 microns and 0.1, respectively. We cloud droplet effective radius of 10

305   microns is expected for stratocumulus clouds over this area (Waquet et al., 2013a). The simulation employs a well-mixed cloud model, where cloud particle properties (e.g., concentration, size) are assumed to be uniform between sea level and cloud top. The same assumption is used for the calculation of heating/cooling rates, see later. Interpolations are performed and a least-square method is used to estimate the COT at 550 nm that best fits the upward shortwave irradiances data.

3.4 Irradiance and heating rates from pyranometer and pyrgeometer measurements

310   Measured shortwave irradiances are first corrected for aircraft attitude (pitch and roll effects) and sensor non-horizontality. A correction for "Air mass" is also applied to the data to compensate for the effects of the variation of the solar angle during

the spiral descent. We refer to Brogniez et al. (2025) for details on these corrections. Data associated with excessively high pitch and roll angles (indicating aircraft turning) are excluded. A polynomial modeling is applied to the profile of net irradiance calculated from downward and upward irradiances. This approach has been used, in particular, to calculate atmospheric heating rates during the ChArMEx campaign over the Mediterranean Sea (Mallet et al., 2016). It enables reducing noise and the creation of a vertical fine sampling of net fluxes, thereby facilitating the calculation of heating rates.

Because of the complex scenes encountered in our study (aerosols above heterogenous low-level clouds) and instrumental noise, the degree of the polynomial fit that best fits the net irradiances profiles was not unique. Polynomials of degrees 6 to 8 have practically similar results in terms of minimizing the correlation coefficient and, consequently, have same accuracy in modeling the net irradiances profiles. However, the heating rates obtained for degrees 6 and 8 exhibit substantial variations. Therefore, we chose to provide a range of possible values for the heating rate by combining the results of the polynomials of degrees 6 to 8. As illustrated in Figures 5 and 6, the uncertainty related to the choice of the polynomial (6, 7, or 8) leads to a variation of approximately 1 K to 1.5 K in the heating rate.

During spiral descents performed above clouds, the radiative properties of the overflown cloud scenes, their albedo, vary continuously during the descent and to a greater or lesser extent depending on the cloud scene studied. Then, the divergence term $dFnet(z)/dz$, which is involved in the calculation of heating rates (Eq. 2), can be considered to be calculated as follows:

$$\frac{dF_{net}(z)}{dz} = \frac{F_{net}(z_2, \rho_2) - F_{net}(z_1, \rho_1)}{z_2 - z_1} \qquad \text{(Eq. 3)}$$

where ρ_1 and ρ_2 are the albedos of the cloudy scenes associated with the net irradiance measurements taken at altitudes z_1 and z_2, respectively.

Airborne irradiance measurements made above clouds during spiral descents are associated with different cloud targets. Thus, the heating rates calculated from the irradiance measurements considered in this study are related to variations in the radiative properties of the atmosphere and also to variations in the radiative properties of the underlying cloud layer. These rates cannot be considered as the "intrinsic" heating rates of the aerosol and atmospheric layers that we seek to calculate and quantify. However, by integrating target albedo variability into the simulations, the heating rates estimated from the measurements will become comparable to the simulated ones. Even if these latter do not reflect the intrinsic properties of the atmosphere, if our theoretical approach, namely the simulations, is able to reproduce the measured heating rates above cloud targets changing at each altitude level z, a fortiori, it will also be able to predict these rates if the cloud target remains fixed (simpler case). The direct comparison of measured and simulated irradiances acquired during the spiral descent will therefore be carried out in a validation perspective. Note that this reasoning applies to measurements acquired in the solar spectrum, with measurements in the thermal infrared appear to unaffected or negligibly affected by this effect.

4 Results

4.1 Sensitivity study utilising GAME simulations

345   A reference case was set for the sensitivity analysis. This reference case is based on a real case study of the field campaign. It represents a typical tropical atmosphere with a cloud top at 1 km. Optical properties used were: Cloud Optical Thickness (COT) 11.69, Aerosol Optical Thickness (AOT) 0.43, and imaginary part of the aerosol complex refractive index 0.03. Fine-mode aerosols are considered between 1-6 km above the 1 km cloud. These values reflect the atmospheric conditions observed just before the start of the aircraft descent performed on the 8th September flight.

350   For particles of the size range shown in table 1, and based on our assumption of spectrally neutral shortwave aerosol absorption (i.e., the aerosol absorption refers to the imaginary part of the complex refractive index and it is assumed to be the same across both the thermal infrared and solar spectrums), the extinction coefficient calculated using Mie theory in the thermal infrared is negligible. This suggests that these biomass burning particles are too small to exert a measurable influence on thermal infrared radiation and their effect in this spectral range is not discussed.

4.1.1 Aerosol and cloud properties

355   Figure 2 presents the primary effects observed on shortwave irradiances and heating/cooling rates based on selected aerosol and cloud properties. Aerosol optical thickness (AOT) significantly impacts both downward and upward fluxes, decreasing as AOT increases (Figures 2a and 2d). Warming rates also increase with AOT, reaching particularly strong values (+8 K/day). These effects are most pronounced in the region where the aerosol layer is placed in the model (between 1 km and slightly below 6 km altitude).

360 Aerosol absorption, another studied parameter (quantified by variations in the imaginary refractive index), reveals that both upward and downward fluxes decrease as absorption increases (Figures 2c, 2f). Heating/cooling rates also rise with aerosol absorption as expected (Figure 2i). With purely scattering particles (i.e., (an imaginary refractive index equal to zero), heating rates remain positive (residual warming from water vapor) but are very low. These simulations confirm aerosol absorption's crucial role in modulating irradiances and heating rates. Accurately representing this parameter, along with aerosol optical thickness, is essential for precise estimates of atmospheric warming rates.

365 The presence of clouds beneath aerosols, primarily characterized by the cloud optical thickness (COT), is another factor considered. The results show that COT has a minimal impact on downward solar flux (Figure 2b). However, due to clouds' significant reflective capacity, their impact on upward solar flux is substantial (Figure 2e). While the choice of cloud optical thickness affects the calculation of heating/cooling rates (Figure 2h), it is less crucial than knowing aerosol optical thickness and absorption.

370
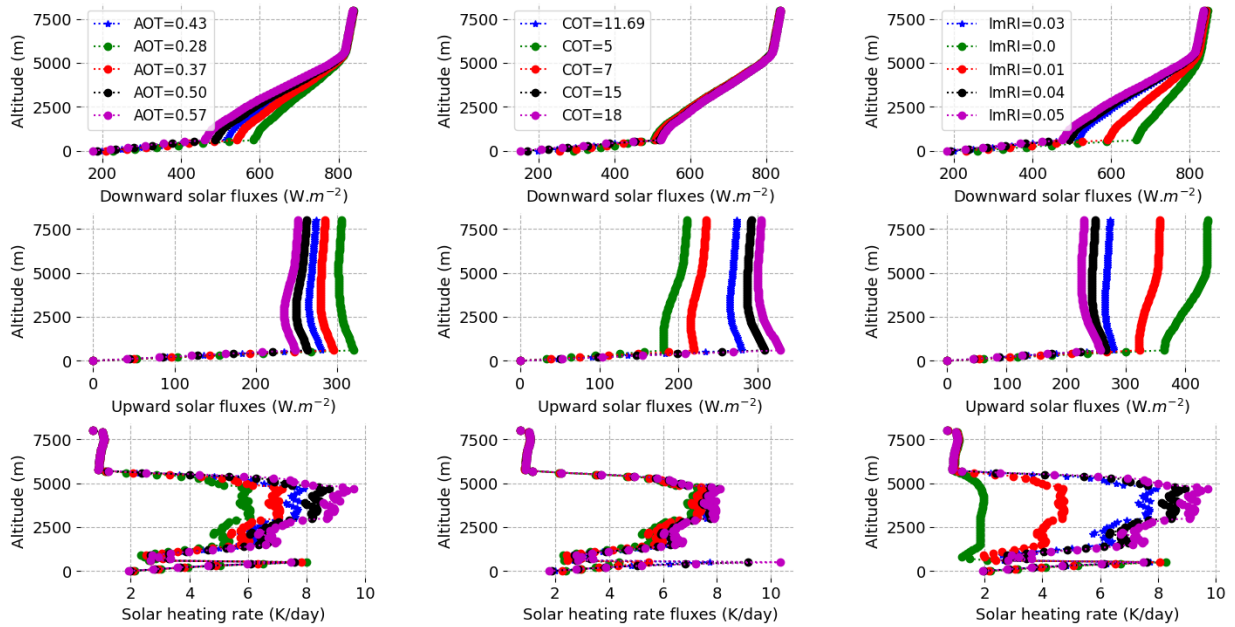
Figure 2: Impact of aerosol and cloud parameter changes on simulated solar radiation: downward (top row), upward irradiances (middle row), and heating/cooling rates (bottom row). Figures a, c and g show the impact of AOT variations. Figures b, e and h show the impact of COT variations. Figures c, f and i show the impact of aerosol absorption variations evaluated by changes in in the aerosol imaginary refractive index referred as "ImRI". The blue curve represents the reference case. The imaginary part of the complex refractive index (see Figure c) of 0., 0.01, 0.03, 0.04 and 0.05 respectively correspond to aerosol single scattering albedo values of 1.00, 0.95, 0.85, 081 and 0.78 at 550 nm.

4.1.2 Water vapor profile

Figure 3 illustrates how irradiance varies with changes in water vapor concentration. The specific humidity profiles used in this analysis are presented in Figure 4c. The profiles obtained by the airborne probe, a dropsonde, and provided by a meteorological reanalysis are shown.

The results shown in Figures 3a and 3b highlight the importance of incorporating a directly measured water vapor profile into the radiative transfer model.

Downward solar irradiances are sensitive to the choice of water vapor profile. We compare the results obtained with reanalysis profiles and the profile measured with the airborne probes. Although re-analysis data is generally reliable, airborne complementary data are crucial for capturing local variations.

390 Figure 3a shows differences in the part of the atmosphere between 1 and 6 km for the downward solar flux. This is explained by the observed differences between the specific humidity profiles observed for the same altitudes (see Fig. 4c and Fig. 4d). Distinctions in simulated downward shortwave irradiances also emerge around 8 km altitude when using reanalysis data or direct measurements. The integrated water vapor content above this altitude differs for the two studied profiles (not shown for clarity, zooming in Figure 4c would be required to see it). Although these quantities are relatively small, these divergences

395 between the profiles are sufficient to explain the observed differences in the simulated downward solar irradiances at this altitude. The presence of water vapor above the aircraft induces a decrease in downward solar radiation. Thus, even a small amount of localized water vapor above the aircraft must be precisely considered in the simulations.

The results obtained in the thermal infrared reveal an even more pronounced sensitivity of fluxes to water vapor. Water vapor contribute to cool the atmosphere in the thermal infrared. One can note cooling of -4 or -6 K depending on the considered

400 profile (Figure 3f). Heating/cooling rated profiles show negative values of -4 to -6 K, with vertical variations depending on the specific profile analyzed. As expected, the cooling is most pronounced at the altitude where water vapor content increases significantly, indicating the influence of the humid smoke layer. It therefore imperative, for calculating the atmospheric heating rates of smoke plumes (aerosol + water vapor), to have precise knowledge of the vertical distribution of water vapor.

405
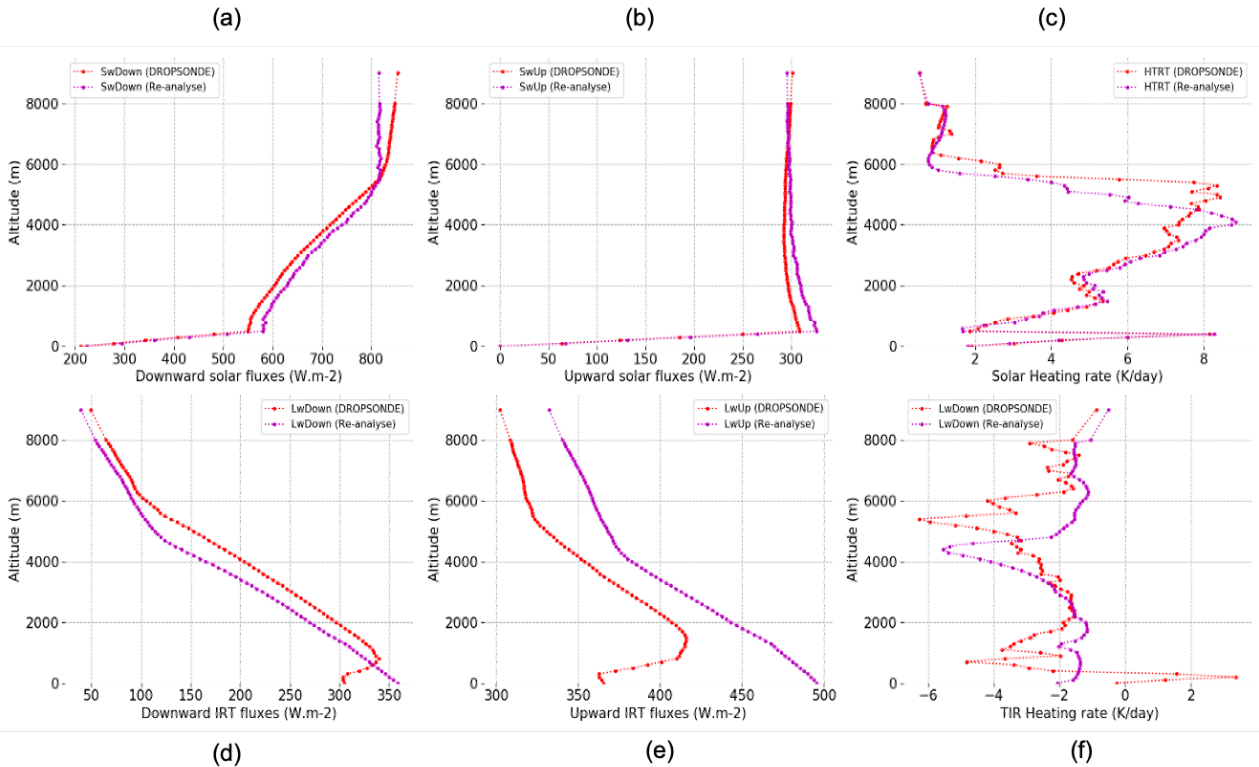
Figure 3: The set of graphs illustrates the impact of the water vapor profile on the upward and downward fluxes in the solar and thermal infrared spectral domains for two different profiles: one obtained from meteorological data (curves in purple) and another acquired during the campaign (curves in red). Profiles of (a) upward shortwave irradiances, (b) downward shortwave irradiances (c) shortwave heating/cooling rates (d) downward thermal infrared irradiances (e) upward thermal infrared irradiances and (f) heating/cooling rates in the thermal infrared.

4.2 Quantifying method accuracy for water vapor and aerosol extinction profiles

Measurements of aerosol optical thicknesses and water vapor taken by PLASMA during the spiral descent were used to validate the extinction and specific humidity profiles used to compute the aerosol heating rates.

Figure 4a shows the extinction profiles retrieved by lidar LNG and OSIRIS before descent (adjusted and unadjusted) on 8th September, 2017. Figure 4b presents the corresponding AOT values compared with the PLASMA AOTs. The combine use of active and passive techniques demonstrates for this case a high degree of success in reconstructing the vertical distribution of aerosol properties within the atmosphere. The minimal impact of the correction term in Eq. 1 suggests a strong similarity between the OSIRIS and lidar LNG retrievals of aerosol properties. It is important to note that this good agreement might not always be achievable when applying this method to spaceborne data. For instance, Deaconu et al. (2019) highlight that significant discrepancies are expected between operational spaceborne POLDER and lidar CALIOP aerosol above clouds optical thicknesses.

As shown in Figure 4c, PLASMA sun-photometer measurements agree well with onboard probe data for water vapor content above 1 km, which is the minimum altitude attained by the aircraft for this particular profile. We have used an instrumental synergy to reconstruct a water vapor profile over the entire atmospheric column (Figure 4-d), which is used in subsequent calculations. The aircraft probe allows the measurement of the water vapor profile between 1 and 8 km (altitudes of the end and beginning of the spiral descent). The dropsonde provides information on the water vapor present in the cloud. A factor is applied to these data to ensure consistency between the aircraft probe measurements and the dropsonde measurements PLASMA measurements are used to check the water vapor content above the aircraft, which is negligible in most cases.
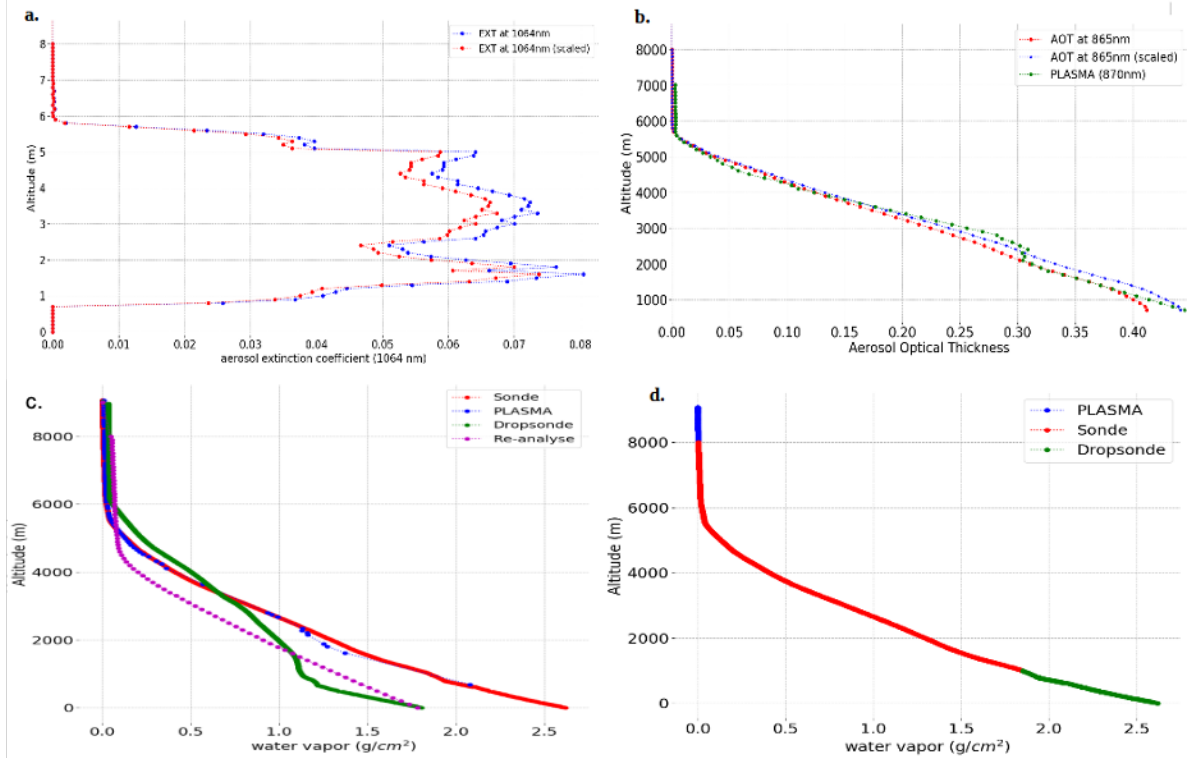
Figure 4: Data for the 8th September flight (a) Aerosol extinction profile measured by the LNG lidar at 1064 nm just before the start of the spiral descent phase. We present results with two approaches: one using the original data and another applying a correction factor to achieve an integrated optical thickness over the entire atmospheric column that matches the value obtained by OSIRIS at 1064 nm. (b) Aerosol optical thickness profile as a function of altitude: PLASMA photometric measurements at 870 nm (in green), calculated profile at 865 nm from lidar retrievals coupled with the estimated particle model with OSIRIS (in blue), calculated profile at 865 nm solely from lidar retrievals (in red). (c)Variation of integrated water vapor content over the air column above the aircraft as a function of altitude, estimated during spiral descents performed with the aircraft, dropsondes, meteorological reanalysis, and PLASMA sun-photometer data. (d) Reconstructed water vapor profile from aircraft sounding, dropsonde, and PLASMA photometer data (see section 4.2).

4.3 Quantifying method accuracy for irradiances and heating rates.

In order to validate the reliability of our methodology, we use the irradiance measurements collected with the pyrgeometer and pyranometer during the vertical spiral descent. Comparing GAME radiative transfer simulations (with inputs of OSIRIS and LNG lidar data) with sounding irradiances will allow evaluating methodology accuracy.

4.3.1 Analysis of fluxes and heating rates

4.3.1-a Case study of 8th September, 2017

450   Figure 5 presents the results obtained for the comparison of measured and simulated fluxes and heating rates for the 8th September 2017 case study. The simulated irradiances (in blue) are shown with their associated error bars. These values come from the error propagation calculations linked to the uncertainties associated with the aerosol parameters retrieved by OSIRIS. The error terms associated with aerosol properties were evaluated based on the work of Chauvigné et al., (2021). We refer to appendix A for details. The measurements are also represented with their uncertainties. We recall that the simulations are based

455   on the OSIRIS and lidar LNG data acquired just before the start of the spiral descent (see the "reference case" described in section 4.1) and reconstructed water profile shown in Figure 4.c.

We observe an excellent agreement between simulations and measurements for this case, both for solar and thermal fluxes. Examining Figure 5, it is noticeable that the measured upward irradiances on the solar spectrum shows significant variations (red curve). These variations, as explained previously, are attributable to the variability of the cloud scenes' properties under

460   the aircraft. The green curve corresponds to solar irradiance calculations from the average cloud optical thickness retrieved during the spiral descent initiation. For the spiral descent, cloud properties need to be recalculated at each change in altitude. During the spiral descent, the majority of COT retrievals fall within the range of 8 to 14. On the blue curve, the retrieval of cloud optical thicknesses with irradiances measurements was performed for each altitude step. The variations due to the presence of the cloud scene were accurately captured with the method described in section 3.3.2, as shown by our graphical

465   comparison.

In the thermal infrared domain, our simulations also manage to reproduce the observed fluxes in a satisfactory manner. The small discrepancies between the measured and simulated fluxes can largely be explained by measurement uncertainties. The comparison was also carried out for the heating rates. We recall that the fluctuations observed on the rates calculated here cannot be considered as solely associated with the variability of the atmospheric properties. The polynomial modeling approach

470   was applied to both the measured and simulated net fluxes, deduced from the upward and downward fluxes presented in Figure 5. This approach allows us to take into account the fact that the albedo of the target present under the aerosol layer is not the same between altitudes z_1 and z_2 (see Eq. 3). By applying this approach, the rates calculated from the measurements and simulations become comparable. For the altitude range associated with the presence of aerosols, the differences between the measured and simulated rates do not exceed 2 K/day, and these differences are within the error bars associated with the

475   calculated rates.
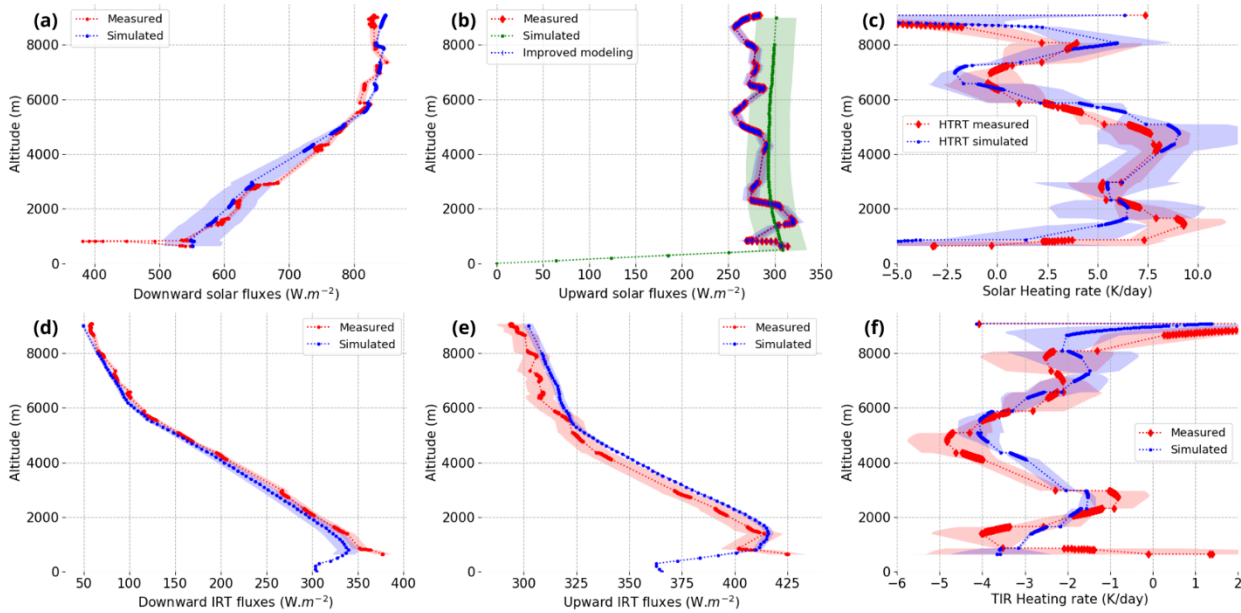
Figure 5: Flux and heating rates as a function of altitude for the thermal infrared and solar domains. Measurements and calculations are performed for the loop descent carried out during the flight of 8th September, 2017. The blue curves represent the simulations, while the red curves correspond to the measurements made during the airborne campaign. The "zones" represented in red and blue correspond to the error bars associated with the measurements and the simulations, respectively. The green curve corresponds to an alternative simulation of the upward solar flux performed for a single cloud optical thickness while this parameter is adjusted for the upward solar flux (blue curve strictly superimposing on the upward solar flux measurement). Profiles of (a) downward shortwave irradiances, (b) upward shortwave irradiances, (c) shortwave heating/cooling rates, (d) downward thermal infrared irradiances (e) upward thermal infrared irradiances and (f) heating/cooling rates in the thermal infrared.

4.3.1-b Case study of 12th September, 2017

The comparisons of the calculated and measured fluxes and rates are shown Figure 6 for the flight performed on 12th September, 2017.

For this second case study, we apply the same protocol as that previously described for the spiral descent performed on 8th September flight, with one exception. The extinction profile retrieved from the polarimeter/lidar synergy was replaced with sun photometer data from PLASMA acquired during the spiral descent. The substitution was made because the region sampled during the spiral descent differed geographically from the high-altitude flight transect where OSIRIS and lidar data were acquired. Simulations were then based on OSIRIS retrievals (i.e. particles size and imaginary refractive index), but AOT came from sun-photometer PLASMA. Compared to the previous case, the cloud properties exhibited greater spatial variability in

495 this second case. Figure 1b illustrates the spatial distribution of the COT along the loop descent path of the 12th September, 2017 flight. On the "east side" of the flight path, COT values exceed 8, while on the "west side" of the loop, COT values are less than 8.

Despite heterogeneity in COT, in the solar domain, the upward irradiances are remarkably well reproduced after adjusting the cloud optical thickness (see differences between green and blue curves in Figure 6). However, larger variations and
500 discrepancies between measurements and simulations are observed for the downward solar flux between 5 and 8 km altitude. Although the sources of these fluctuations are not fully identified, our main hypothesis is that the spatial variability of atmospheric properties in the region above the aircraft could be responsible. Thus, the large loop radius, variations in the spatial distribution of atmospheric properties above the aircraft, and potentially the presence of high clouds could explain these fluctuations. Errors in the corrections applied to the flux measurements cannot be ruled out. However, on average, the simulated
505 downward flux falls between the maximum and minimum measured flux values. There is very good agreement between the measured and simulated heating rates for spectral solar calculations, despite significant profile variations due to cloud scene variability.

In the thermal infrared domain, the measured and simulated irradiances exhibit remarkable agreement, showing a consistent order of magnitude. The simulated heating rates also show good agreement in terms of order of magnitude with the
510 measured rates. However, a significant difference of the order of 2 K/day between the simulated and measured heating rates is observed between 4 and 6 km and also between 6 and 8 km. This significant discrepancy can be attributed to the observed discrepancies in the upward and downward fluxes, measured and simulated, for this altitude range. During rapid descents with the aircraft, irradiance measurements in the thermal infrared can be affected (Meloni et al., 2018). When thermal equilibrium between the ambient air, the sensor's window, and the instrument is not achieved, the flux measurements performed in the
515 thermal infrared range can be biased (Albrecht et al., 1974; Curry and Herman, 1985). This behavior has already been reported and constitutes our primary explanatory hypothesis for the departure observed here between our measured data and simulation results.
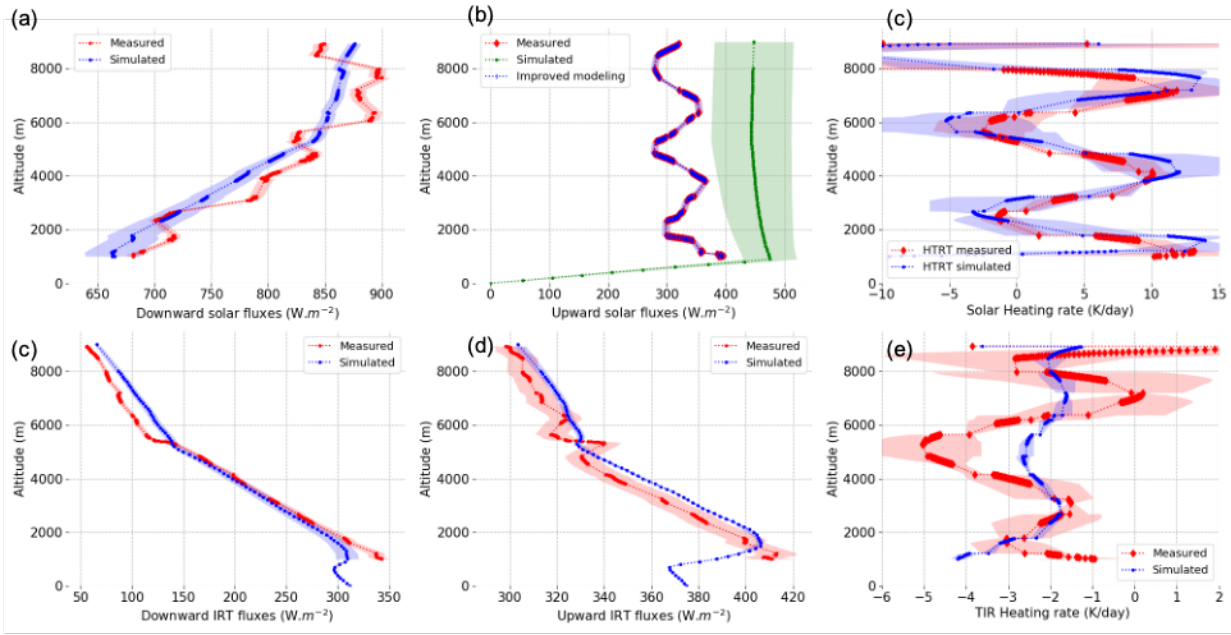
Figure 6. Same as Figure 5 for the flight of 12th September, 2017.

4.4 Mimicking satellite remote sensing: active-passive data synergy from high-altitude flights' measurements

In this section, we analyze atmospheric heating/cooling rates profiles retrieved using OSIRIS and lidar LNG data acquired during high-altitude flight segments (8-10 km).

4.4.1 Estimation of cooling/warming rates for 8 and 12th September flights

Figure 7 (first column) shows the heating/cooling rates obtained with this approach as a function of acquisition time for the 8th September flight. We show the profiles of the aerosol attenuated backscattering coefficient at 1064 nm in function of altitude (Fig. 7.a), the atmospheric heating/cooling rates calculated in the solar spectrum (Fig 7.c), the "aerosol-specific" heating rate (Fig 7.e), the atmospheric heating/cooling rates calculated in the thermal infrared spectrum and finally, the global atmospheric heating rate, calculated from the sum of the solar and infrared irradiances. The "aerosol-specific" heating rate quantifies the specific contribution of aerosols to atmospheric heating. It can only be estimated by a radiative transfer calculation. The calculations are performed twice, with and without aerosols. The heating rate calculated in the presence of aerosols is corrected for the calculation performed without aerosols, providing what we will call the aerosol heating rate.

Overall, we observe good spatial homogeneity in the results of the calculated rates for both the atmosphere and aerosols. The main observable flaw in these results is the presence of strong values of heating rates at the top of the aerosol layer, which are all found in all rate calculations (> 10 K/day). This corresponds to clouds forming at the top of the aerosol layer. In the context of developing an operational space product, these values should be filtered. This problem disappears between 8:15 and

8:2 (decimal UTC time). For 12th September, no cloud formation was observed at the top of the aerosol layer (see Figure 7b). Missing data in heating rate figures for this second flight (Figures 7d, g, h and j) result from missing available OSIRIS data or retrievals. Average AOT at 865 nm was 0.45 and 0.18 respectively on the 8th and 12th September, explaining the lower 1064-nm backscatter for the 12th September flight (see Figures 7a and 7b). Similar key findings were observed for both flights. The results of the 8th September flight are discussed below.

Over the solar spectrum, we find the order of magnitude of the heating rates estimated during the spiral descent, presented in the previous section. This is particularly the case at the end of the axis, which corresponds to the flight section carried out just before the spiral descent. For the atmospheric rates calculated on the solar spectrum, we note higher values in the top of the smoke layer, which is due to water vapor, as explained in the sensitivity study section. For aerosol heating rates, we observe fairly homogeneous values of the order of 4 to 5 K/day between 1 km and 6 km approximately.

The profiles of heating rates in the thermal infrared do not show any variability as a function of acquisition time. A single and unique specific humidity profile is used for the calculations and this one which sets the vertical variability on this parameter. We recall that the effect of biomass burning aerosols is almost negligible in our calculation in the thermal infrared (see discussion section 4.1). The only possible spatial variations are here linked to the properties of the low-level cloud (mostly changes in the altitude of the cloud top).

We observe that the calculated thermal infrared warming rates are very close to the warming rates estimated from the measurements. For example, the calculated cooling rate in the upper part of the layer (-4K/day) is clearly visible in the rates previously estimated using the pyrgeometer for similar altitudes (see Figure 6f around -5K/day between 4 and 6 km). A similar cooling at a comparable altitude is also confirmed by the analysis performed for the 7th September profile (not shown), which corroborates this result.

While the atmospheric global heating/cooling rates account for all radiative processes (solar and infrared), they are rather comparable to the heating rates derived solely from aerosols. This suggests that water vapor's influence on solar and thermal radiation tends to offset each other, resulting in a relatively neutral effect on average throughout the atmosphere.

560
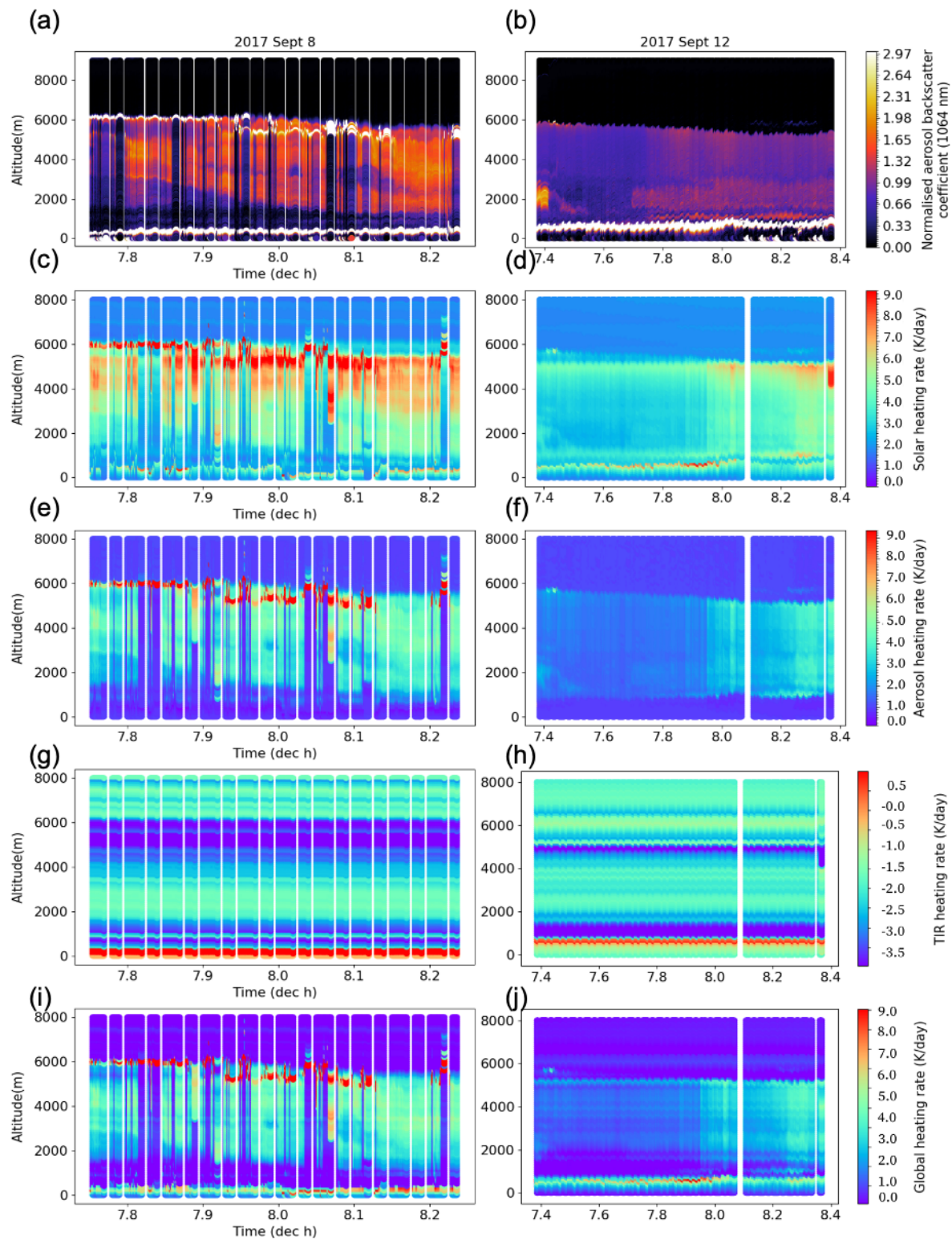
Figure 7. Heating rates calculated above clouds as a function of acquisition time and data provided by the LNG lidar. Results for the for the flight of 8th September, 2017 are shown in the left column. Results for the 12th September, 2017 are show in the right column. (a) and (b) attenuated backscatter coefficient measured at 1064 nm, (c) and (d) atmospheric heating rates calculated over the solar spectrum (e) and (f) specific aerosol heating rates calculated over the solar spectrum (g) and (f) heating (cooling) rate calculated in the thermal infrared and (i) and (j) global atmospheric heating rate (solar + thermal infrared).

4.4.2 Assessment of heating/cooling rates above clouds for the AEROCLO-sA campaign

Figure 8 presents averaged vertical profiles of atmospheric heating/cooling rates, specific aerosol heating rates, water vapor, and aerosol extinction for the 5, 7, 8, 9 and 12th September flights. The mean cloud top altitude is also reported (horizontal black line). The plots shown in Figure 8 are ranked by decreasing heating rate.

Different scenarios of biomass burning aerosols above clouds are evident in the extinction profiles (Figure 8, orange curves). On 7th September, two distinct aerosol layers are visible: one near the cloud top (1 km) and another between 4 and 6 km. A transition zone, with less aerosol extinction and heating, separates these two layers (Fig. 8d, between 2 and 4 km,). For 12th September, only one main aerosol layer is visible, starting from the cloud top (1 km). This suggests that aerosols might be within the cloud or at least in contact with the cloud top for this case. A strong correlation is also observed between the aerosol extinction and specific humidity profiles. On 9th September, same strong correlation between water vapor and aerosol extinction can be noted for altitudes higher than 3 km (see Fig. 8) with a peak in both profiles around 3.5 km. Below 3 km, water vapor and aerosol extinction appear anti-correlated.

On 7th and 12th September, aerosol-induced atmospheric heating is occurring just above the cloud layer. For the other cases, there is generally a distinct transition zone (area with no or few aerosols) between the cloud top and the base of the layer and the maximum heating occurs at higher altitudes than the cloud top altitude.

The estimated aerosol-induced heating rates above the clouds vary from 2 to 5 K/day on average depending on the observation day and aerosol optical thickness (see Table 3). The table 3 contains the vertically integrated values of the heating rates. The aerosol-specific heating and global heating/cooling rate profiles calculated in our study are generally very close. Therefore, both quantities can be used to constrain the warming of biomass burning plumes observed during AEROCLO-sA. This confirms a relatively neutral global (solar + thermal infrared) effect of water vapor on solar and thermal infrared radiation spectra, at least on average over the vertical profile, which is the case for the values given in Table 3. Cooling due to water vapor in the thermal is about -2K on average (see table 3). Locally, as we have seen in earlier discussion (see the sensitivity study section), water vapor can accentuate the cooling occurring at the top of the aerosol layer (see Figure 8c and 8d, respectively for the 9 and 7 Sept. flights around 6 km). For the 5 and 7th September flights, a slight increase in global rates can be noted compared to the rates calculated only for aerosols, suggesting a slightly positive water vapor balance for these cases.
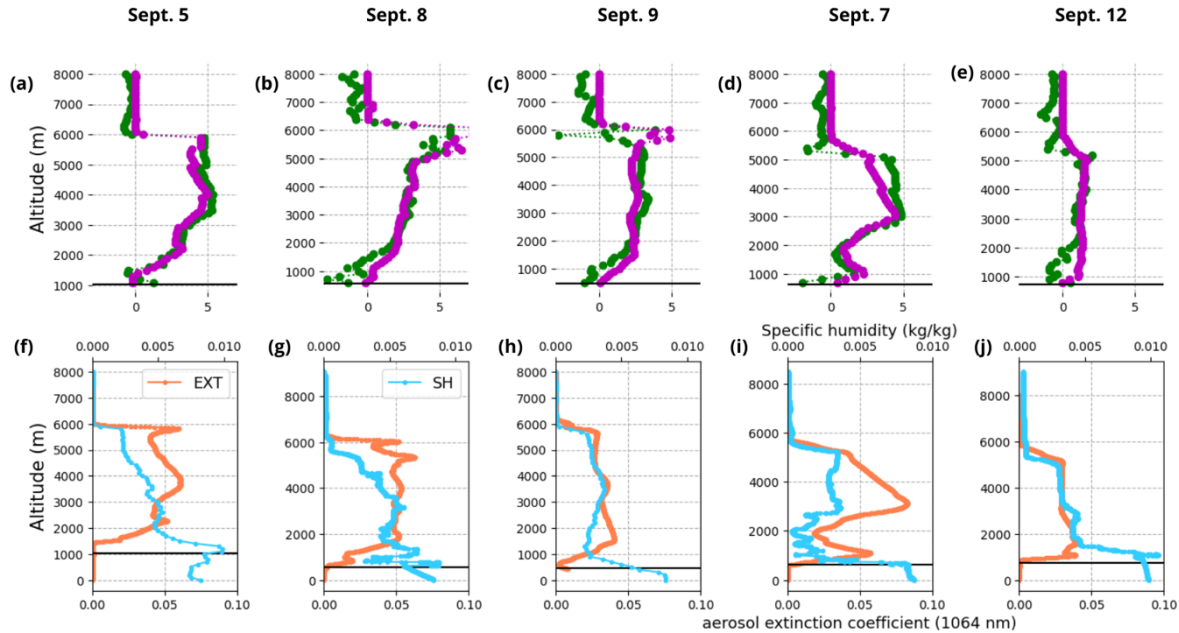
Figure 8: Mean values of vertical profiles heating/cooling rates above clouds for the 5, 8, 9, 7 and 12th September flights. The first line shows the global heating/cooling rates (curves in green) and the aerosol-specific heating rates (curves in purple) as a function of altitude and flight's day. The second line represents the associated mean profiles of specific humidity in Kg/Kg (curves in blue, top axis) and aerosol extinction at 1064 nm in 10^{-3} Km^{-1} unit (orange curves, bottom axis). The horizontal black line indicates the mean cloud top altitude.

Heating rate (K/day)	Sept. 5 AOT = 0.57	Sep. 8 AOT = 0.45	Sept. 9 AOT = 0.30	Sept. 7 AOT = 0.24	Sept. 12 AOT = 0.18
Solar	+ 7.20	+ 7.11	+ 6.34	+ 5.77	+ 3.73
Thermal infrared	- 2.34	- 2.50	- 2.42	- 2.33	- 2.16
Global	+ 4.86	+ 4.60	+ 3.91	+ 3.53	+ 1.57
Aerosol only	+ 4.58	+ 4.35	+ 3.68	+ 3.03	+ 1.80

Table 3: Presentation of the average values computed over the vertical for heating/cooling rates for the various above clouds' flight segments of the AEROCLO-sA campaign. The mean AOT values at 865 nm for each flight are also reported.

5 Conclusions and perspectives

Aerosol-induced atmospheric heating plays a key role in shaping the dynamics of biomass burning plumes, influencing their vertical distribution, transport, and the dynamic and properties of the low-level clouds.

We developed an innovative approach that combines airborne measurements from OSIRIS polarimeter and LNG lidar to derive aerosol heating rates and global atmospheric heating rates incorporating water vapor. To calculate these quantities, we also utilize a radiative transfer code and additional meteorological parameters provided by radiosondes.

This methodology is assessed during massive transports of biomass burning particles observed during the September 2017 AEROCLO-sA airborne campaign in Namibia.

The spiral descent performed with the aircraft allowed for the acquisition of detailed vertical profiles of irradiances, aerosol optical thickness (measured by PLASMA), and water vapor directly within the plumes. These data were essential for enabling a measurement-based calculation of heating rates, allowing for validation of a unique dimension of the methodology. For the first time, atmospheric heating rates calculated using a radiative transfer code were compared to heating rates directly measured in the atmosphere. Above clouds, estimating shortwave heating rates from irradiance measurements presented challenges due to the rapid variation in the properties of the underlying target (the cloud). However, a comparison between the rates directly derived from irradiance measurements and those estimated from the synergy between OSIRIS and the LNG lidar was achieved. This approach, based on airborne irradiance measurements thus allowed for the assessment of the active-passive synergy method robustness. Overall, the results showed good agreement between the heating rates and their uncertainties from measurements and calculations (error bar overlap) mostly.

This good agreement between measurements and calculations also underscores the importance of the rigorous methods employed and flights strategy. These methods include minimizing pitch and roll during flight maneuvers (spiral descent) and applying appropriate corrections to the irradiance measurements (Brogniez et al., 2025). To fully utilize these specialized measurements, homogeneous atmospheric conditions are also necessary. Subsequently, analyzing the collected data allows for selecting the descents that achieve the desired scientific objectives.

The aerosol specific heating rates (vertically averaged) are positive and vary between +2 K/day and +5 K/day. As noted in previous studies (Pistone et al., 2021), aerosol and water vapor distribution are often correlated within these smoke plumes. Within the smoke layer, for water vapor, the warming effect in the shortwave is generally compensated by cooling in the longwave. However, an exception occurs at the top of the layer, where a stronger cooling effect of -1.5 K/day often dominates due to water vapor, with potential impact on high-level clouds formation. Our estimates are in good agreement to those obtained during the ORACLES campaign (2-8 K/day, Cochrane et al., 2022). Nevertheless, the global (solar + thermal) atmospheric heating/cooling rates computed above clouds are weaker than in Cochrane et al. (2022) who did not consider the influence of

640   water vapor in the thermal infrared. The specific aerosol heating rates estimates are close as the observed particles primarily interact with the shortwave radiations. Deaconu et al., (2019) used CALIOP and aerosol above clouds POLDER products to estimate aerosol above cloud heating rates. Their study near the coast of Angola showed values of 5.7 K.day^{-1} for aerosol heating rates above clouds, which is also coherent with our results.

A recent study based on the Meso-NH model demonstrated the importance of heating rates on the dynamics of biomass
645   burning aerosol plumes observed during the AEROCLO-sA campaign (Chaboureau et al., 2022). It would be especially valuable to adjust the heating rates in the model based on our results. This would allow us to verify if the adjusted model more accurately reproduces the altitudes of the base and top of the smoked layers. This work could lead to better modeling of the aerosol transport and dynamics in this region. Based on these results, one of the objectives will be also to compare observational inversions of the heating rate due to smoke with the output of the ALADIN model over this region (Mallet et al. 2019).
650   In the long term, our major perspective is the generalization of this method to the global level. The approach presented here based on the synergy of airborne active and passive remote sensing measurements, could be applied, with some adjustments, to space-based lidar and polarimeter. Especially, the water vapor and temperature profiles provided here by the dropsonde or probes could be provided by meteorological reanalysis.

As demonstrated in our simulations, the choice of the cloud optical thickness of the target underlying the aerosol layer has
655   an impact on the calculation of heating rates, although its impact is minimal compared to its influence on calculating the direct forcing of aerosols above clouds (De Graaf et al., 2020). Accounting for cloud optical thickness, with corrections applied to address how the presence of the lofted aerosol layer affects the retrieval of cloud properties (as done in Peers et al., 2015), could be valuable for this purpose.

Mineral dust particles should be also included in our method since dust are also usually observed above clouds at regional
660   scale (Waquet et al., 2013b). Mineral coarse particles significantly interact with thermal infrared radiation and their optical properties will have to be accounted for in the algorithm.

Furthermore, our current method assumes constant aerosol properties (size, complex refractive index, and single scattering albedo) with altitude. However, observations suggest that SSA varies with altitude within biomass burning layers (Wu et al., 2020). As our method currently only considers variable above-cloud aerosol concentration as a function of the altitude,
665   incorporating altitude-dependent aerosol properties could enhance its accuracy.

By considering these important points and leveraging the capabilities of satellite instruments, the method could be extended for current and future satellite-based measurements. There are currently five years of satellite retrievals of aerosol properties above clouds, referred as the AEROsol Above-Clouds (AERO-AC) products (Waquet et al., 2020), including above cloud aerosol SSA, AOT and cloud corrected optical thicknesses, from the POLDER/PARASOL mission data, which can be used in
670   synergy with CALIOP lidar data (Deaconu et al., 2019). Our approach could be also applied to future European missions such as 3MI and the Earth Clouds, Aerosols and Radiation Explorer (EarthCARE) satellite (Wher et al., 2023) and also the Atmosphere Observing System (AOS) mission (Gettelman et al., 2021), that also plans to combine passive and active instruments in space. This will enable a more comprehensive analysis of aerosol-cloud-radiations interactions on a regional

and global scale, contributing to a better understanding of climate processes and improved climate models for better climate change predictions.

Appendix A

The GAME code is used to perform error propagation calculations to provide a range of possible solutions for irradiances and heating/cooling rate estimates. The error terms associated with aerosol properties were evaluated based on the work of Chauvigné et al., (2021). The relative error is estimated to be 10% for the aerosol optical thickness (AOT estimated by OSIRIS) at 865 nm (expressed as a relative value). The error on the aerosol imaginary refractive index is 0.005 and the error on aerosol size (radius) is 0.02 microns. It is not easy to validate the cloud thickness retrievals, so the error was estimated to be 2 for the cloud optical thickness. Calculations are performed using the below equation for estimating errors in irradiances.

$$\sigma_{Flux}(z) = \sqrt{\sum_i \left(\frac{\partial Flux(z, X_i)}{\partial X} \times \sigma_{X_i} \right)^2} \qquad \text{(Eq. 1-A)}$$

where σ_{X_i} stands for the error associated with each individual parameter. A similar formula is sued for the errors computed for the heating/cooling rate.

Data availability.

Fill in using DOI provided for each dataset on baobab

Author contributions

Competing interests

At least one of the (co-)authors is a member of the editorial board of Atmospheric Measurement Techniques. Moreover, Paola Formenti is guest editor for the ACP Special Issue "New observations and related modelling studies of the aerosol–cloud–climate system in the Southeast Atlantic and southern Africa regions". The remaining authors declare that they have no conflicts of interests.

Special issue statement

705 This article is part of the special issue "New observations and related modelling studies of the aerosol–cloud–climate system in the Southeast Atlantic and southern Africa regions (ACP/AMT inter-journal SI)". It is not associated with a conference.

Acknowledgments

Airborne data were obtained using the aircraft managed by SAFIRE (http://www.safire.fr, last access: 11 May 2021), the
710 French facility for airborne research, and infrastructure of the French National Centre for Scientific Research (CNRS), Météo-France, and the French National Centre for Space Studies (CNES). The AEROCLO-sA database is maintained by the French national data centre for atmospheric data and services, AERIS. The strong diplomatic assistance of the French Embassy in Namibia, the administrative support of the Service Partnership and Valorisation of the Regional Delegation of the Paris–Villejuif region of the CNRS, and the cooperation of the Namibian National Commission on Research, Science, and
715 Technology (NCRST) were invaluable in making the project happen.

Financial support

The AEROCLO-sA project has been supported by the French National Research Agency (grant no. ANR-15-CE01-0014-01), the French national program LEFE/INSU, the Programme national de Télédetection Spatiale (PNTS;; grant no. PNTS-2016-14), the French National Agency for Space Studies (CNES), and the South African National Research Foundation (NRF; grant
720 no. 105958). The research leading to these results has received funding from the European Union's Seventh Framework Programme (FP7/2014-2018) under the EUFAR2 (grant no. 312609). Aurélien Chauvigné and Fabien Waquet acknowledge the additional financial support provided by the Programme national de Télédétection Spatial (PNTS; grant no. PNTST-2020-06).

Mégane Ventura and Fabien Waquet also acknowledge support from the CaPPA project (Chemical and Physical Properties of
725 the Atmosphere), which is funded by the French National Research Agency (ANR) through the PIA (Programme d'Investissement d'Avenir; grant 80 no. ANR-11-LABX-0005-01) and by the Conseil Régional Hauts-de-France and the European Funds for Regional Economic Development (FEDER).

References

Albrecht, B., Poellot, M., and Cox, S.: Pyrgeometer measurements from aircraft. Rev. Sci. Instrum., 45, 33–38,
730   doi:10.1063/1.1686443, 1974.

Bellouin, N., Quaas, J., Gryspeerdt, E., Kinne, S., Stier, P., Watson-Parris, D., Boucher, O., Carslaw, K.S., Christensen, M.,
    Daniau, A.-L., Dufresne, J.-L., Feinglod, G., Fiedler, S., Forster, P., Gettelman, A., Haywood, J.M., Lohmann, U.,
    Malavelle, F., Maurotsen, T., McCoy, D.T., Myhre, G., mülmenstädt, J., Neubauer, D., Possner, A., Rugenstein, M.,

Sato, Y., Schulz, M., Scharts, S.E., Sourdeval, O., Storelvmo, T., Toll, V., Winker, D., Stevens, B. (2020). Bounding global aerosol radiative forcing of climate change. Rev. Geophys., 58(1), e2019RG000660.

Costantino, L. and Bréon, F. M.: Aerosol indirect effect on warm clouds over South-East Atlantic, from co-located MODIS and CALIPSO observations, Atmos. Chem. Phys., 13(1), 69–88, doi:10.5194/acp-13-69-2013, 2013.

Brogniez G., Waquet F., Ventura M. and F. Parol. (2025). Analysis and development of procedures for correcting airborne broadband irradiances measurements. From raw measurements to geophysical products. J*ournal of Quantitative Spectroscopy and Radiative Transfer, special issue on Peter C. Waterman Award*, under review.

Chaboureau, J.-P., Labbouz, L., Flamant, C., and Hodzic, A.: Acceleration of the southern African easterly jet driven by the radiative effect of biomass burning aerosols and its impact on transport during AEROCLO-sA, Atmos. Chem. Phys., 22, 8639–8658, https://doi.org/10.5194/acp-22-8639-2022, 2022.

Chauvigné, A., Waquet, F., Auriol, F., Blarel, L., Delegove, C., Dubovik, O., Flamant, C., Gaetani, M., Goloub, P., Loisil, R., Mallet, M., Nicolas, J.-M., Parol, F., Peers, F., Torres, B., and Formenti, P.: Aerosol above-cloud direct radiative effect and properties in the Namibian region during the AErosol, RadiatiOn, and CLOuds in southern Africa (AEROCLO-sA) field campaign – Multi-Viewing, Multi-Channel, Multi-Polarization (3MI) airborne simulator and sun photometer measurements, Atmos. Chem. Phys., 21, 8233–8253, https://doi.org/10.5194/acp-21-8233-2021, 2021.

Cochrane, S. P., Schmidt, K. S., Chen, H., Pilewskie, P., Kittelman, S., Redemann, J., LeBlanc, S., Pistone, K., Segal Rozenhaimer, M., Kacenelenbogen, M., Shinozuka, Y., Flynn, C., Ferrare, R., Burton, S., Hostetler, C., Mallet, M., and Zuidema, P.: Biomass burning aerosol heating rates from the ORACLES (ObseRvations of Aerosols above CLouds and their intEractionS) 2016 and 2017 experiments, Atmos. Meas. Tech., 15, 61–77, https://doi.org/10.5194/amt-15-61-2022, 2022.

Curry, J. A. and Herman, G. F.: Infrared radiative properties of summertime Arctic stratus clouds, J. ClimateAppl. Meteor., 24, 525–538, doi:10.1175/1520- 0450(1985) 024<0525: IRPOSA>2.0.CO;2,1985.

Deaconu, L. T., Waquet, F., Josset, D., Ferlay, N., Peers, F., Thieuleux, F., Ducos, F., Pascal, N., Tanré, D., Pelon, J. and Goloub, P.: Consistency of aerosols above clouds characterization from A-Train active and passive measurements, Atmos. Meas. Tech, 10, 3499–3523, doi:10.5194/amt-10-3499-2017, 2017.

Deaconu, L. T., Ferlay, N., Waquet, F., Peers, F., Thieuleux, F., and Goloub, P.: Satellite inference of water vapour and above-cloud aerosol combined effect on radiative budget and cloud-top processes in the southeastern Atlantic Ocean, Atmos. Chem. Phys., 19, 11613–11634, https://doi.org/10.5194/acp-19-11613-2019, 2019.

De Graaf, M., Schulte, R., Peers, F., Waquet, F., Tilstra, L. G., and Stammes, P.: Comparison of south-east Atlantic aerosol direct radiative effect over clouds from SCIAMACHY, POLDER and OMI–MODIS, Atmos. Chem. Phys., 20, 6707–6723, https://doi.org/10.5194/acp-20-6707-2020, 2020.

Denjean C., T. Bourrianne, F. Burnet, M. Mallet, N. Maury, A. Colomb, P. Dominutti, J. Brito, R. Dupuy, K. Sellegri, A. Schwarzenboeck, C. Flamant, P. Knippertz, Overview of aerosol optical properties over Southern West Africa from DACCIWA aircraft measurements. Atmos. Chem. Phys. 20, 4735–4756 (2020).

Dubuisson, P., J. C. Roger, M. Mallet et O. Dubovik (2006). "A code to compute the direct solar radiative forcing: application to anthropogenic aerosols during the Escompte experiment". In : Proc. International Radiation Symposium (IRS 2004) on Current Problems in Atmospheric Radiation, edited by : Fischer, H., Sohn, B.-J., and Deepak, A., Hampton, p. 127–130.

Flamant, C., Gaetani, M., Chaboureau, J.-P., Chazette, P., Cuesta, J., Piketh, S. J., and Formenti, P.: Smoke in the river: an Aerosols, Radiation and Clouds in southern Africa (AEROCLO-sA) case study, Atmos. Chem. Phys., 22, 5701–5724, https://doi.org/10.5194/acp-22-5701-2022, 2022.

Formenti, P., D'Anna, B., Flamant, C., Mallet, M., Piketh, S. J., Schepanski, K., Waquet, F., Auriol, F., Brogniez, G., Burnet, F., Chaboureau, J.-P., Chauvigné, A., Chazette, P., Denjean, C., Desboeufs, K., Doussin, J.-F., Elguindi, N., Feuerstein, S., Gaetani, M., Giorio, C., Klopper, D., Mallet, M. D., Nabat, P., Monod, A., Solmon, F., Namwoonde, A., Chikwililwa, C., Mushi, R., Welton, E. J., and Holben, B.: The aerosols, radiation and clouds in southern Africa. Field campaign in Namibia: Overview, illustrative observations and way forward. Bull. Amer. Meteor. Soc., 100, nº 7, 1277-1298. https://doi.org/10.1175/BAMS-D-17-0278.1, 2019.

Forster, P., V. Ramaswamy, P. Artaxo, T. Berntsen, R. Betts, D.W. Fahey, J. Haywood, J. Lean, D.C. Lowe, G. Myhre, J. Nganga, R. Prinn, G. Raga, M. Schulz and R. Van Dorland, 2007: Changes in Atmospheric Constituents and in Radiative Forcing. In: Climate Change 2007: The Physical Science Basis. Contribution of Working Group I to the Fourth Assessment Report of the Intergovernmental Panel on Climate Change [Solomon, S., D. Qin, M. Manning, Z. Chen, M. Marquis, K.B. Averyt, M.Tignor and H.L. Miller (eds.)]. Cambridge University Press, Cambridge, United Kingdom and New York, NY, USA.

Fougnie Bertrand, Thierry Marbach, Antoine Lacan, Ruediger Lang, Peter Schlüssel, Gabriele Poli, Rosemary Munro, André B. Couto, The multi-viewing multi-channel multi-polarisation imager – Overview of the 3MI polarimetric mission for aerosol and cloud characterization, Journal of Quantitative Spectroscopy and Radiative Transfer, Volume 219, 2018, Pages 23-32, ISSN 0022-4073, https://doi.org/10.1016/j.jqsrt.2018.07.008.

Gettelman, A., Carmichael, G. R., Feingold, G., Da Silva, A. M., & Van den Heever, S. C. (2021). Confronting future models with future satellite observations of clouds and aerosols. *Bulletin Of The American Meteorological Society*, *102*, E1557-E1562. doi:10.1175/BAMS-D-21-0029.1

Haywood, J. M., Abel, S. J., Barrett, P. A., Bellouin, N., Blyth, A., Bower, K. N., Brooks, M., Carslaw, K., Che, H., Coe, H., Cotterell, M. I., Crawford, I., Cui, Z., Davies, N., Dingley, B., Field, P., Formenti, P., Gordon, H., de Graaf, M., Herbert, R., Johnson, B., Jones, A. C., Langridge, J. M., Malavelle, F., Partridge, D. G., Peers, F., Redemann, J., Stier, P., Szpek, K., Taylor, J. W., Watson-Parris, D., Wood, R., Wu, H., and Zuidema, P.: The CLoud–Aerosol–Radiation Interaction and Forcing: Year 2017 (CLARIFY-2017) measurement campaign, Atmos. Chem. Phys., 21, 1049–1084, https://doi.org/10.5194/acp-21-1049-2021, 2021.

IPCC, 2022: Climate Change 2022: Impacts, Adaptation, and Vulnerability. Contribution of Working Group II to the Sixth Assessment Report of the Intergovernmental Panel on Climate Change [H.-O. Pörtner, D.C. Roberts, M. Tignor, E.S.

Poloczanska, K. Mintenbeck, A. Alegría, M. Craig, S. Langsdorf, S. Löschke, V. Möller, A. Okem, B. Rama (eds.)]. Cambridge University Press. Cambridge University Press, Cambridge, UK and New York, NY, USA, 3056 pp., doi:10.1017/9781009325844.

805   Jethva, H., Torres, O., Waquet, F., Chand, D., and Hu, Y.: How do A-train sensors intercompare in the retrieval of above-cloud aerosol optical depth? A case study-based assessment, Geophys. Res. Lett., 41, 186–192, https://doi.org/10.1002/2013GL058405, 2014.

Jethva, H., Torres, O., and Ahn, C.: A 12-year long global record of optical depth of absorbing aerosols above the clouds derived from the OMI/OMACA algorithm, Atmos. Meas. Tech., 11, 5837–5864, https://doi.org/10.5194/amt-11-5837-810   2018, 2018.

Jethva, H. T., Torres, O., Ferrare, R. A., Burton, S. P., Cook, A. L., Harper, D. B., Hostetler, C. A., Redemann, J., Kayetha, V., LeBlanc, S., Pistone, K., Mitchell, L., and Flynn, C. J (2024), Retrieving UV–Vis spectral single scattering albedo of absorbing aerosols above clouds from synergy of ORACLES airborne and A-train sensors, Atmos. Meas. Tech., 17, 2335–2366, https://doi.org/10.5194/amt-17-2335-2024.

815   Johnson, B. T., Shine, K. P., and Forster, P. M.: The semi-direct aerosol effect: Impact of absorbing aerosols on marine stratocumulus, Q. J. Roy. Meteor. Soc., 130, 1407–1422, https://doi.org/10.1256/qj.03.61, 2004.

Karol, Y., Tanré, D., Goloub, P., Vervaerde, C., Balois, J. Y., Blarel, L., Podvin, T., Mortier, A., and Chaikovsky, A.: Airborne sun photometer PLASMA: concept, measurements, comparison of aerosol extinction vertical profile with lidar, Atmos. Meas. Tech., 6, 2383–2389, https://doi.org/10.5194/amt-6-2383-2013, 2013.

820   Keil, A., and J. M. Haywood, Solar radiative forcing by biomass burning aerosol particles during SAFARI 2000: A case study based on measured aerosol and cloud properties, J. Geophys. Res., 108(D13), 8467, doi:10.1029/2002JD002315, 2003.

Klett, J. D., "Stable Analytical Inversion Solution for Processing Lidar Returns," Applied Optics, vol. 20, pp. 211–220, 1981. https://doi.org/10.1364/AO.20.000211.

Lack, D. A., J. M. Langridge, R. Bahreinia, C. D. Cappa, A. M. Middlebrook, 825   and J. P. Schwarz (2012), Brown carbon and internal mixing in biomass burning particles, P. Natl. Acad. Sci. USA, doi:10.1073/pnas.1206575109.

Lu, Z., Liu, X., Zhang, Z., Zhao, C., Meyer, K., Rajapakshe, C., et al. (2018). Biomass smoke from Southern Africa can significantly enhance the brightness of stratocumulus over the southeastern Atlantic Ocean. *Proceedings of the National Academy of Sciences of the United States of America*, 115(12), 2924–2929. https://doi.org/10.1073/pnas.1713703115

830   Brian I. Magi, Qiang Fu, Jens Redemann, Beat Schmid, Using aircraft measurements to estimate the magnitude and uncertainty of the shortwave direct radiative forcing of southern African biomass burning aerosol, Journal of Geophysical Research: Atmospheres, 10.1029/2007JD009258, 113, D5, (2008).

Mallet, M., Dulac, F., Formenti, P., Nabat, P., Sciare, J., Roberts, G., Pelon, J., Ancellet, G., Tanré, D., Parol, F., Denjean, C., Brogniez, G., di Sarra, A., Alados-Arboledas, L., Arndt, J., Auriol, F., Blarel, L., Bourrianne, T., Chazette, P., 835   Chevaillier, S., Claeys, M., D'Anna, B., Derimian, Y., Desboeufs, K., Di Iorio, T., Doussin, J.-F., Durand, P., Feron,

A., Freney, E., Gaimoz, C., Goloub, P., Gomez-Amo, J. L., Granados-Muñoz, M. J., Grand, N., Hamonou, E., Jankowiak, I., Jeannot, M., Léon, J.-F. Maillé, M., Mailler, S., Meloni, D., Menut, L., Momboisse, G., Nicolas, J., Podvin, T., Pont, V., Rea, G., Renard, J.-B., Roblou, L., Schepanski, K., Schwarzenboeck, A., Sellegri, K., Sicard, M., Solmon, F., Somot, S., Torres, B., Totems, J., Triquet, S., Verdier, N., Verwaerde, C., Waquet, F., Wenger, J., and Zapf, P.,: Overview of theChemistry-Aerosol MediterraneanExperiment/Aerosol DirectRadiativeForcingontheMediterraneanClimate (ChArMEx/ADRIMED) summer 2013 campaign. Atmos. Chem. Phys., 16, 455-504, doi:10.5194/acp-16-455-2016, 2016.

Mallet, M., Nabat, P., Zuidema, P., Redemann, J., Sayer, A. M., Stengel, M., Schmidt, S., Cochrane, S., Burton, S., Ferrare, R., Meyer, K., Saide, P., Jethva, H., Torres, O., Wood, R., Saint Martin, D., Roehrig, R., Hsu, C., and Formenti, P., Simulation of the transport, vertical distribution, optical properties and radiative impact of smoke aerosols with the ALADIN regional climate model during the ORACLES-2016 and LASIC experiments, Atmos. Chem. Phys., 19, 4963-4990, 2019.

Mallet Marc, Fabien Solmon, Pierre Nabat, Nellie Elguindi, Fabien Waquet, Dominique Bouniol, Andrew Mark Sayer, Kerry Meyer, Romain Roehrig, Martine Michou, Paquita Zuidema, Cyrille Flamant, Jens Redemann, and Paola Formenti Atmos. Chem. Phys., 20, 13191–13216, https://doi.org/10.5194/acp-20-13191-2020, 2020.

Mallet, M., P. Nabat, B. Johnson, M. Michou, J. M. Haywood, C. Chen and O. Dubovik, Climate models generally underrepresent the warming by Central Africa biomass-burning aerosols over the Southeast Atlantic., Sci. Adv., 7, eabg9998, 2021.

Meloni, D., di Sarra, A., Brogniez, G., Denjean, C., De Silvestri, L., Di Iorio, T., Formenti, P., Gómez-Amo, J. L., Gröbner, J., Kouremeti, N., Liuzzi, G., Mallet, M., Pace, G., and Sferlazzo, D. M.: Determining the infrared radiative effects of Saharan dust: a radiative transfer modelling study based on vertically resolved measurements at Lampedusa. Atmos. Chem. Phys., 18, 4377-4401. doi.org/10.5194/acp-18-4377-2018, 2018.

Meyer, K., S. Platnick, L. Oreopoulos, and D. Lee (2013), Estimating the direct radiative effect of absorbing aerosols overlying marine boundary layer clouds in the southeast Atlantic using MODIS and CALIOP, J. Geophys. Res. Atmos., 118, 4801–4815, doi:10.1002/jgrd.50449.

Peers, F., F. Waquet, C. Cornet, P. Dubuisson, F. Ducos, P. Goloub, F. Szczap, D. Tanré, et F. Thieuleux. 2015. « Absorption of Aerosols above Clouds from POLDER/PARASOL, Measurements and Estimation of Their Direct Radiative Effect ». Atmospheric Chemistry and Physics 15 (8): 4179-96. https://doi.org/10.5194/acp-15-4179-2015.

Peers, F., Bellouin, N., Waquet, F., Ducos, F., Goloub, P., Mollard, J., Myhre, G., Skeie, R. B., Takemura, T., Tanré, D., Thieuleux, F., and Zhang, K.: Comparison of aerosol optical properties above clouds between POLDER and AeroCom models over the South East Atlantic Ocean during the fire season, Geophys. Res. Lett., 43, 3991–4000, https://doi.org/10.1002/2016GL068222, 2016.

Peers, F., Francis, P., Fox, C., Abel, S. J., Szpek, K., Cotterell, M. I., Davies, N. W., Langridge, J. M., Meyer, K. G., Platnick, S. E., and Haywood, J. M.: Observation of absorbing aerosols above clouds over the south-east Atlantic Ocean from

870   the geostationary satellite SEVIRI – Part 1: Method description and sensitivity, Atmos. Chem. Phys., 19, 9595–9611, https://doi.org/10.5194/acp-19-9595-2019, 2019.

Pilewskie, P., J. Pommier, R. Bergstrom, W. Gore, S. Howard, M. Rabbette, B. Schmid, P. V. Hobbs, and S. C. Tsay (2003), Solar spectral radiative forcing during the Southern African Regional Science Initiative, J. Geophys. Res., 108, 8486, doi:10.1029/2002JD002411, D13.

875 Pistone K., J. Redemann, S. Doherty, P. Zuidema, S. Burton, B. Cairns, S. Cochrane, R. Ferrare, C. Flynn, S. Freitag, S. G. Howell, M. Kacenelenbogen, S. LeBlanc, X. Liu, S. Schmidt, A. J. Sedlacek, M. Segal-Rozenhaimer, Y. Shinozuka, S. Stamnes, B. van Diedenhoven, G. Van Harten, G. F. Xu, Intercomparison of biomass burning aerosol optical properties from in situ and remote-sensing instruments in ORACLES-2016. Atmos. Chem. Phys. 19, 9181–9208 (2019).

Pistone, K., Zuidema, P., Wood, R., Diamond, M., da Silva, A. M., Ferrada, G., Saide, P. E., Ueyama, R., Ryoo, J.-M., Pfister,
880   L., Podolske, J., Noone, D., Bennett, R., Stith, E., Carmichael, G., Redemann, J., Flynn, C., LeBlanc, S., Segal-Rozenhaimer, M., and Shinozuka, Y.: Exploring the elevated water vapor signal associated with the free tropospheric biomass burning plume over the southeast Atlantic Ocean, Atmos. Chem. Phys., 21, 9643–9668, https://doi.org/10.5194/acp-21-9643-2021, 2021.

Redemann, J., Wood, R., Zuidema, P., Doherty, S. J., Luna, B., LeBlanc, S. E., Diamond, M. S., Shinozuka, Y., Chang, I. Y.,
885   Ueyama, R., Pfister, L., Ryoo, J.-M., Dobracki, A. N., da Silva, A. M., Longo, K. M., Kacenelenbogen, M. S., Flynn, C. J., Pistone, K., Knox, N. M., Piketh, S. J., Haywood, J. M., Formenti, P., Mallet, M., Stier, P., Ackerman, A. S., Bauer, S. E., Fridlind, A. M., Carmichael, G. R., Saide, P. E., Ferrada, G. A., Howell, S. G., Freitag, S., Cairns, B., Holben, B. N., Knobelspiesse, K. D., Tanelli, S., L'Ecuyer, T. S., Dzambo, A. M., Sy, O. O., McFarquhar, G. M., Poellot, M. R., Gupta, S., O'Brien, J. R., Nenes, A., Kacarab, M., Wong, J. P. S., Small-Griswold, J. D., Thornhill, K.
890   L., Noone, D., Podolske, J. R., Schmidt, K. S., Pilewskie, P., Chen, H., Cochrane, S. P., Sedlacek, A. J., Lang, T. J., Stith, E., Segal-Rozenhaimer, M., Ferrare, R. A., Burton, S. P., Hostetler, C. A., Diner, D. J., Seidel, F. C., Platnick, S. E., Myers, J. S., Meyer, K. G., Spangenberg, D. A., Maring, H., and Gao, L.: An overview of the ORACLES (ObseRvations of Aerosols above CLouds and their intEractionS) project: aerosol–cloud–radiation interactions in the southeast Atlantic basin, Atmos. Chem. Phys., 21, 1507–1563, https://doi.org/10.5194/acp-21-1507-2021, 2021.

895 Sakaeda, N., Wood, R., and Rasch, P. J.: Direct and semidirect aerosol effects of southern African biomass burning aerosol, J. Geophys. Res., 116, D12205, https://doi.org/10.1029/2010JD015540, 2011.

Siméon, A., Waquet, F., Péré, J.-C., Ducos, F., Thieuleux, F., Peers, F., Turquety, S., and Chiapello, I.: Combining POLDER-3 satellite observations and WRF-Chem numerical simulations to derive biomass burning aerosol properties over the southeast Atlantic region, Atmos. Chem. Phys., 21, 17775–17805, https://doi.org/10.5194/acp-21-17775-2021, 2021.

900 Solomon, Susan, Martin Manning, Melinda Marquis, et Dahe Qin. 2007. Climate change 2007- the physical science basis: Working group I contribution to the fourth assessment report of the IPCC. Vol. 4. Cambridge university press.

Solmon, F., Elguindi, N., Mallet, M. *et al.* West African monsoon precipitation impacted by the South Eastern Atlantic biomass burning aerosol outflow. *npj Clim Atmos Sci* **4**, 54 (2021). https://doi.org/10.1038/s41612-021-00210-w.

Stier, P., N. a. J. Schutgens, N. Bellouin, H. Bian, O. Boucher, M. Chin, S. Ghan, et al. 2013. « Host Model Uncertainties in Aerosol Radiative Forcing Estimates: Results from the AeroCom Prescribed Intercomparison Study ». Atmospheric Chemistry and Physics 13 (6): 3245-70. https://doi.org/10.5194/acp-13-3245-2013.

Trenberth, Kevin E., John T. Fasullo, et Jeffrey Kiehl. 2009. « Earth's Global Energy Budget ». Bulletin of the American Meteorological Society 90 (3): 311-24. https://doi.org/10.1175/2008BAMS2634.1.

Waquet, F., J. Riedi, L. C. Labonnote, P. Goloub, B. Cairns, J-L. Deuzé, et D. Tanré. 2009. « Aerosol Remote Sensing over Clouds Using A-Train Observations ». Journal of the Atmospheric Sciences 66 (8): 2468-80. https://doi.org/10.1175/2009JAS3026.1 .

Waquet, F., C. Cornet, J.-L. Deuzé, O. Dubovik, F. Ducos, P. Goloub, M. Herman, et al. 2013a. « Retrieval of Aerosol Microphysical and Optical Properties above Liquid Clouds from POLDER/PARASOL Polarization Measurements ». Atmospheric Measurement Techniques 6 (4): 991-1016. https://doi.org/10.5194/amt-6-991-2013.

Waquet, F., F. Peers, F. Ducos, P. Goloub, S. Platnick, J. Riedi, D. Tanré, et F. Thieuleux. 2013b. « Global analysis of aerosol properties above clouds ». Geophysical Research Letters 40 (21): 5809-14. https://doi.org/10.1002/2013GL057482 .

Waquet F., Peers F., Ducos F., Thieuleux F., Deaconu L., A. Chauvigné and Riedi, J.: Aerosols above clouds products from POLDER/PARASOL satellite observations (AERO-AC products), doi:10.25326/82, 2020. (https://www.icare.univ-lille.fr/aero-ac/)

Wehr, T., Kubota, T., Tzeremes, G., Wallace, K., Nakatsuka, H., Ohno, Y., Koopman, R., Rusli, S., Kikuchi, M., Eisinger, M., Tanaka, T., Taga, M., Deghaye, P., Tomita, E., and Bernaerts, D.: The EarthCARE mission – science and system overview, Atmos. Meas. Tech., 16, 3581–3608, https://doi.org/10.5194/amt-16-3581-2023, 2023.

Wilcox, E. M.: Stratocumulus cloud thickening beneath layers of absorbing smoke aerosol, Atmos. Chem. Phys., 10(23), 11769–11777, doi:10.5194/acp-10-11769-2010, 2010.

Wu H., J. W. Taylor, K. Szpek, J. M. Langridge, P. I. Williams, M. Flynn, J. D. Allan, S. J. Abel, J. Pitt, M. I. Cotterell, C. Fox, N. W. Davies, J. Haywood, H. Coe, Vertical variability of the properties of highly aged biomass burning aerosol transported over the southeast Atlantic during CLARIFY-2017. Atmos. Chem. Phys. 20, 12697–12719 (2020).

Zhang, Z., Meyer, K., Yu, H., Platnick, S., Colarco, P., Liu, Z., and Oreopoulos, L.: Shortwave direct radiative effects of above-cloud aerosols over global oceans derived from 8 years of CALIOP and MODIS observations, Atmos. Chem. Phys., 16, 2877–2900, https://doi.org/10.5194/acp-16-2877-2016, 2016.

Zuidema, Paquita, Ping Chang, Brian Medeiros, Ben P. Kirtman, Roberto Mechoso, Edwin K. Schneider, Thomas Toniazzo, et al. 2016a. « Challenges and Prospects for Reducing Coupled Climate Model SST Biases in the Eastern Tropical Atlantic and Pacific Oceans: The U.S. CLIVAR Eastern Tropical Oceans Synthesis Working Group ». Bulletin of the American Meteorological Society 97 (12): 2305-28. https://doi.org/10.1175/BAMS-D-15-00274.1.

Zuidema, Paquita, Jens Redemann, James Haywood, Robert Wood, Stuart Piketh, Martin Hipondoka, et Paola Formenti. 2016b. « Smoke and Clouds above the Southeast Atlantic: Upcoming Field Campaigns Probe Absorbing Aerosol's Impact on Climate ». Bulletin of the American Meteorological Society 97 (7): 1131-35. https://doi.org/10.1175/BAMS-

D-15-00082.1.

Zuidema P., A. J. Sedlacek III, C. Flynn, S. Springston, R. Delgadillo, J. Zhang, A. Aiken, A. Koontz, P. Muradyan, The
940  Ascension Island boundary layer in the remote southeast Atlantic is often smoky. Geophys. Res. Lett. 45, 4456–4465
  (2018).

945